



---

# Submillimeter stacking analyses of optically selected galaxies

---

THESIS

submitted in partial fulfillment of the  
requirements for the degree of

MASTER OF SCIENCE  
in  
ASTRONOMY

Author :

S.T.M. Schouws

Supervisor :

Dr. J.A.Hodge

Leiden, The Netherlands, January 20, 2017



# Submillimeter stacking analyses of optically selected galaxies

**S.T.M. Schouws**

Leiden Observatory, Leiden University  
P.O. Box 9513, 2300 RA Leiden, The Netherlands

January 20, 2017

## **Abstract**

This research presents a stacking analysis of color selected galaxies and galaxies selected by their physical parameters. The stacking analysis on color selected galaxies confirms previous results and demonstrates the effectiveness of the used stacking methods.

Stacking on physically selected galaxies is used to determine the molecular masses and subsequently the gas fractions of those stacked galaxies.

It is observed that the gas fraction increases with redshift. Higher mass galaxies have a higher gas fraction and galaxies with a larger specific star formation rate with respect to the main sequence also have a higher gas fraction. There seems to be tentative evidence for different evolution for different galaxies.

Finally, the molecular mass as determined from the dust continuum method used in this work is compared to masses derived from CO based methods. A discrepancy of a factor  $\sim 2.5\text{-}3$  is found. This is in accordance with other studies and requires further explanation.



# Contents

<b>1</b>	<b>Introduction</b>	<b>1</b>
1.1	Cosmic star formation history	1
1.2	Light from galaxies	3
1.2.1	MAGPHYS	5
1.3	Color selection	5
1.4	Stacking analysis	6
1.4.1	Weighted mean stacking	6
1.4.2	Global deblending	8
1.5	Molecular gas mass from continuum observations	11
1.6	This research	13
<b>2</b>	<b>Color selected galaxies</b>	<b>15</b>
2.1	Previous work	15
2.2	Method	17
2.2.1	Submillimeter datasets	17
2.2.2	Catalog and color selection	18
2.2.3	Stacking methods	19
2.2.4	Size measurement	21
2.3	Results	23
2.3.1	LESS	23
2.3.2	ALMA	23
2.4	Discussion	30
2.4.1	LESS	30
2.4.2	ALMA	30
2.4.3	Overall discussion	32
2.5	Conclusion	33

<b>3</b>	<b>Gas fraction of galaxies selected by physical properties</b>	<b>35</b>
3.1	Previous work	35
3.2	Method	37
3.2.1	Submillimeter datasets	37
3.2.2	Catalog	37
3.2.3	SED fitting	38
3.2.4	Stacking methods	39
3.2.5	Molecular gas masses	39
3.3	Results	41
3.3.1	ALESS	41
3.3.2	LESS and HerMES	41
3.4	Discussion	58
3.4.1	Grid binning	58
3.4.2	Stellar mass dependence	59
3.4.3	Dependence on $sSFR_{ms}$	60
3.4.4	Comparison with CO based gas fractions	61
3.5	Conclusion	63
<b>4</b>	<b>Conclusion</b>	<b>65</b>
4.0.1	Future work	66

# Introduction

## 1.1 Cosmic star formation history

The universe was a very different place back at high redshifts. The current epoch is a relatively calm period in cosmic history and it will only get calmer, but this report is not concerned with that gloomy future. Instead, it is interesting to look back and observe the growth of structure.

This growth of structure started very tentatively, as is observable in the minute temperature differences in the earliest observable light. This light not only shows the seeds of all later structure, it also reveals the energy contents of the universe. Knowing the build-up of the universe is essential to be able to make predictions about the growth of structure.

The current best cosmological model is the  $\Lambda$  Cold Dark Matter ( $\Lambda$ CDM) model, which predicts a hierarchical growth of increasingly large structures. A growth which is dominated by dark matter where normal matter only plays a small role. But everything that is known about the universe results from observing this puny fraction of everything there is.

Moreover, only a small part of the normal matter is in the form of stars. The rest of the normal matter is located in-between stars, galaxies or even clusters of galaxies. It is from this gas that stars form.

Star formation has not always been tranquil as it is today, with a few exceptions, local galaxies form much less stars than galaxies at higher redshifts, this is illustrated in figure 1.1. The star formation rate (SFR) in galaxies appears to be a function of redshift.

It is possible to look at the star formation rate for galaxies with different masses and different redshifts. For an example of such a study, see figure 1.2. It is striking that the SFR is observed to increase with redshift for the complete mass range. Moreover, all galaxies seem to be located around

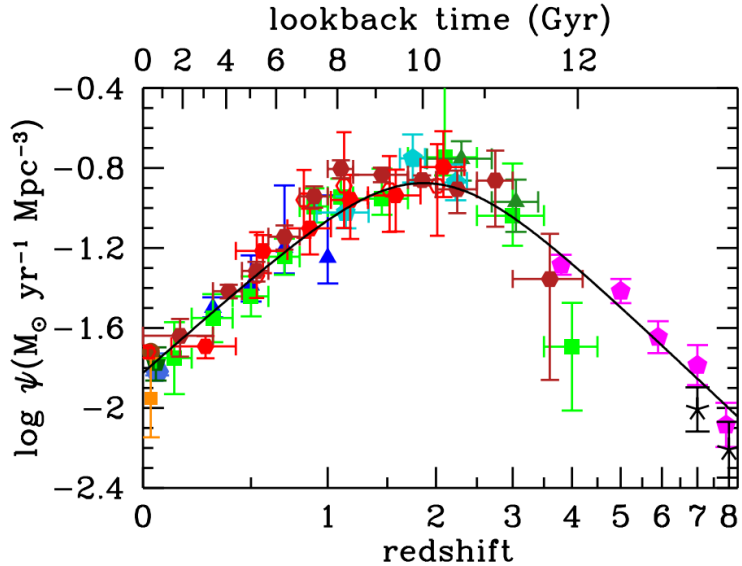


**Figure 1.1:** Comoving star formation rate density as a function of redshift. Data-points are taken from a large number of studies and combine measurements in the UV and IR. Adapted from Madau & Dickinson (2014) (figure 9).

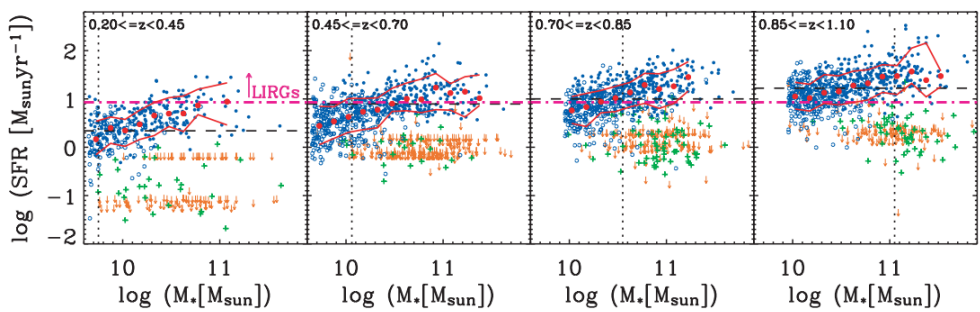


**Figure 1.2:** Star formation rate (SFR) as a function of stellar mass for different redshift ranges. A line is drawn for galaxies that at low redshifts would be classified as Luminous InfraRed Galaxies (LIRGs). Adapted from Noeske et al. (2007) (figure 1).

a line that increases with redshift, this relation between stellar mass, star formation rate and redshift is called the main sequence of star forming galaxies (Noeske et al. 2007). More recent studies have observed this main sequence at much higher redshifts (e.g. Schreiber et al. (2015)).

In the local universe galaxies with very high star formation rates and subsequently high infrared luminosity are called Luminous Infrared Galaxies (LIRGs) or even Ultra Luminous InfraRed Galaxies (ULIRGs). As can be seen from figure 1.2, most galaxies at  $z > 1$  would actually be classified as LIRGs. It is therefore better to classify galaxies according to their excess star formation with respect to the main sequence. Especially since only about  $\sim 2\%$  of galaxies has a specific star formation rate ( $sSFR = SFR/M_*$ ) higher than  $\sim 4 \times$  the star formation rate of the main sequence (Scoville et al. 2016).

This tightness of the main sequence for all redshifts indicates that normal star formation is probably not driven by frequent random burst caused by mergers for example. Furthermore, it seems that galaxies on the main sequence at high redshifts look similar to normal star forming galaxies at  $z=0$ , despite having orders of magnitude higher star formation rates (Schreiber et al. 2015).

The mechanism behind star formation on main sequence galaxies is not yet understood (Schreiber et al. 2015). Although it is likely that the availability of cold gas plays an important role. It is observed that the gas fraction ( $f_{gas} = M_{mol}/(M_{mol} + M_*)$ ) increases with redshift. It is also observed that despite these larger gas fractions, the gas consumption timescales are relatively short (e.g. Scoville et al. (2016)).

To keep the star formation going, the gas needs to be replenished. From simulations it is expected that this replenishment is achieved through cold flows of gas Carilli & Walter (2013). However, these simulations are complicated and need to take into account feedback processes from supernovae and active galactic nuclei. Moreover, observationally these cold flows will be difficult to detect (Kimm et al. 2011).

## 1.2 Light from galaxies

Despite the previously discussed main sequence, galaxies are much more varied than for example stars, which entire life-cycle is predetermined by their mass. There are galaxies with very high masses, these are often elliptical with old populations of stars and virtually no gas. Galaxies with low stellar masses also exist, for example the Magellanic Clouds, are gas rich.

Any galaxy consists of several components. One of the most obvious

---

components are the stars. Stars are formed with different initial masses and the fraction of stars that is formed for a certain mass can be modelled by an initial mass function. A well known example is the Chabrier (2003) initial mass function (IMF).

Very massive stars have a short lifetime, but in that lifetime they dominate the stellar luminosity distribution. Especially the energy emitted in the UV part of the spectrum by these stars is important. On the other hand, low mass stars live for much longer, but are also less luminous. These low mass stars dominate the stellar mass of a galaxy and can be observed in the near infrared (NIR). This is one of the reasons that rest-frame NIR bands can be used to estimate the stellar mass of a galaxy.

Because stars of different ages emit different kinds of light, the complete spectral energy distribution (SED) of a galaxy can tell a lot about the stellar population and subsequently the history of that galaxy. Moreover, if there is much UV light and thus young stars, it is clear that that galaxy has been forming stars up until very recently. This is the reason that rest-frame UV light is often used as a measure of the star formation rate of a galaxy.

Though not only stars contribute to the SED of galaxies. Galaxies also contain gas and dust and the amount of these depends on redshift. At optical and UV wavelengths, dust can absorb light. This influences estimates of the star formation rate of galaxies. The energy they absorb heats the dust and is re-emitted at longer wavelengths, which depends on the temperature of the dust.

Gas also contributes to the SED of a galaxy, most of the gas consists of ionized, neutral or molecular hydrogen. This gas can be observed through line emission. Other elements also play important roles for the study of galaxies, specifically the molecule carbon mono-oxide (CO). This is the second most abundant molecule in the inter stellar medium (ISM) and can be observed really well through its rotational transitions in the radio and submillimeter, whereas molecular hydrogen is much more difficult to observe.

There are also much larger molecules in the ISM, especially polycyclic aromatic hydrocarbons (PAHs). These molecules have broad emission features in the mid infrared (MIR).

### 1.2.1 MAGPHYS

As described above, there are a lot of properties of galaxies that leave their imprints on the SED of these galaxies. Henceforth, it is possible to look at the light from a galaxy and deduce its physical properties.

One of the methods to estimate the properties of a galaxy is by fitting the observed SED. MAGPHYS (da Cunha et al. 2008) is one of the model packages that makes such an analysis possible and it will be used later on in this report.

MAGPHYS uses a sophisticated model of light in galaxies and with this model thousands of SEDs for a large variety of parameters are calculated. To compare these models to an observed galaxy, it is necessary to know the redshift of that galaxy. The expected fluxes at that redshift from every model are then compared to the actual observed fluxes. From comparing with all model SEDs, a marginalized likelihood distribution of each physical parameter of the observed galaxy is generated. This distribution gives the estimated physical parameters for the observed galaxy.

One of the advantages of MAGPHYS is the fact that it uses one consistent model to describe the model SEDs from the UV to the far infrared (FIR), in contrast to more limited models. Another advantage is the limited amount of computation required to fit a galaxy, it can thus be used to model the physical properties of a large number of galaxies. The latter is essential for the work described in this report.

## 1.3 Color selection

Color selection is the method to use photometric colors to select for general physical properties of interest without having to resort to the observation of expensive spectra. For the work described in this report, the sBzK, ERO and DRG color selection schemes are used. These color selection methods complement other similar techniques like UV selection and Lyman-break galaxies to obtain a more complete census of galaxies at high redshifts. To be specific, UV selection and Lyman-break galaxies do not select for dusty red high redshift galaxies.

A very simple color selection criterion is used to select for Extremely Red Objects (ERO) (Thompson et al. 1999). Selection for red colors selects galaxies with an old stellar population or star forming galaxies that contain a lot of dust at high redshifts. Specifically, with the aid of spectroscopy, it was shown that the ERO color selection selects for old passive galaxies at  $0.8 < z < 2$  and dusty star forming galaxies at similar redshifts (Cimatti

et al. 2003). Though it has also been found that most ERO galaxies reside at  $z \sim 1$ , with a smaller fraction at higher redshifts (Daddi et al. 2004).

To select for galaxies at higher redshifts, selection criteria using the  $J$  and  $K$  NIR bands were developed. One of these selection methods calls selected objects Distant Red Galaxies (DRG) (Franx et al. 2003). It was found that this criterion is effective at selecting high redshift galaxies, most of which are reddened star forming objects (van Dokkum et al. 2004). Though, still a significant portion of the galaxies selected via this method is located at  $z \sim 1$  (Daddi et al. 2004).

The BzK is another well known color selection method. It was specifically developed to select for dust reddened galaxies at  $1.4 < z < 2.5$  (Daddi et al. 2004). The acronym BzK stands for the photometric  $B, z$  and  $K$  bands used in the definition of this color selection. The definition was chosen such that it runs parallel with the reddening vector, that way galaxies are selected irrespective of their dust extinction. Additionally, the BzK criterion additionally distinguishes between star forming galaxies (sBzK) and passively evolving galaxies (pBzK). It was found that sBzK galaxies tend to have a significantly higher star formation rate than EROs (Daddi et al. 2004).

## 1.4 Stacking analysis

If the flux of a class of objects is below the noise threshold of a dataset, stacking analysis can be used to lower the noise floor by combining (*stacking*) the flux of a number of sources. See for example figure 1.3. In order for this kind of analysis to be possible, the positions of the sources of interest need to be known in advance from prior detections at other wavelengths. Since a large number of sources is combined, only the average properties of the class of sources are preserved. Stacking analysis has been used from the X-ray regime to the radio (e.g. Caillault & Helfand (1985) and Georgakakis et al. (2003) respectively). There are several ways to perform a stacking analysis, using the median is very popular as it reduces the impact of bright outliers. Another method that is often used is weighted mean stacking. This stacking method will be discussed briefly below.

### 1.4.1 Weighted mean stacking

At the position of a source of interest (target), the flux value of the nearest pixel  $f_{target}$  can be measured and a weight  $w_{target}$  can be assigned to this pixel. A common choice for  $w_{target}$  is the square of the pixel noise  $1/\sigma_{target}^2$ .

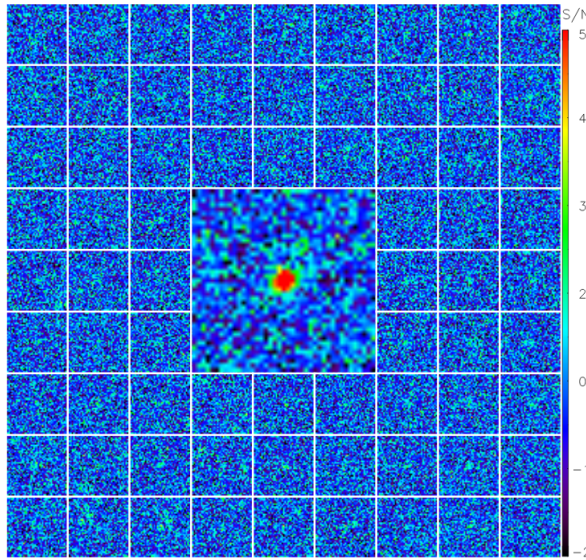


**Figure 1.3:** Example of a simulated stacking analysis. In the small panels cutouts around known source positions are shown, individual sources are not detected. In the large central panel the stacked image is displayed, the stacked emission has a SNR of  $\sim 10$ . Adapted from Avendano (2015) (figure 4.3).

The pixel noise can for example be obtained from a weight map. Next, a weighted average over all targets is taken as the value of the stacked flux:

$$\langle I_{targets} \rangle = \frac{\sum w_{target} f_{target}}{\sum w_{target}} \quad (1.1)$$

Here  $\langle I_{targets} \rangle$  is the stacked submillimeter flux and  $f_{target}$  is the flux of a stacking source with weight  $w_{target}$ . The noise of the stacked image can be determined from the weights of the pixels:

$$\langle \sigma_{targets} \rangle = \frac{1}{\sum w_{target}} \quad (1.2)$$

If the noise of all pixels would be equal,  $\sigma_i = \sigma$ , then the signal-to-noise ratio (SNR) would decrease with the square of the number of target sources ( $N$ ) in the stack:  $SNR \propto 1/\sqrt{N}$ . However, this is only the case when the stacked fluxes are uncorrelated. For example when the point spread functions (PSF's) of several sources overlap (blending), the stacking analysis described in this section will overestimate the true flux of the targets.

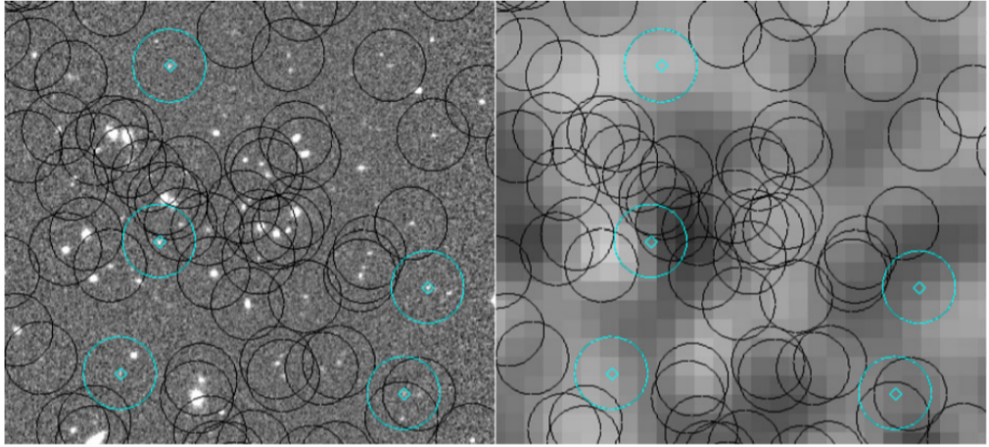


**Figure 1.4:** Left panel: Cutout from a  $K$ -band image of the ECDFS. Right panel: A  $870\mu\text{m}$  image of the same region from the LESS survey. The black circles have a radius of  $\sim 12$  arcseconds and correspond to sources which are part of the  $K < 20$  sample as determined from MUSYC photometry. Cyan circles indicate sBzK sources, as an example of sources of interest for a stacking analysis. Adapted from Kurczynski & Gawiser (2010) (figure 1).

This section focussed only on stacking on the fluxes of single pixels, however this method can be easily expanded to stacking on cutouts by treating every individual pixel in the cutout as described in this section.

#### 1.4.2 Global deblending

As described in the previous section, if the PSF's of several sources overlap to contribute to the flux measured in a pixel (see for example figure 1.4), the weighted mean stacking method will overestimate the flux of the target sample. In order to perform a stacking analysis on data with a very low resolution compared to the source catalog used for the source selection, a different method is needed. A promising method is described by Kurczynski & Gawiser (2010), the idea behind this method will be described in this section and will henceforth be referred to as the global deblending method.

The global deblending method is similar to conventional stacking methods where the flux of adjacent neighbouring sources is deconvolved. More sophisticated methods additionally consider neighbours of neighbours (Greve et al. 2010). The global deblending method takes this idea one step further and does not limit the deblending to neighbours or neighbours of neighbours, but instead considers the effect of all sources on all other sources.

The first step in any stacking analysis is to select a several subsamples ( $G_1, G_2\dots$ ) of length ( $N_1, N_2\dots$ ) containing sources ( $g_{1,1}, g_{1,2}\dots$ ) from a catalog. It is important that a source only belongs to one subsample. The sources not belonging to any subsample form a subsample themselves ( $G_0$ ). The purpose of a stacking analysis is to measure the fluxes from every subsample ( $I_0, I_1, I_2\dots$ ).

The flux at the position of a random source ( $g_{x,y}$ ) from subsample  $G_x$  can be given by the following expression:

$$\sigma_{g_{x,y}} + I_0 \sum_j^{N_0} \alpha_{g_{x,y}, g_{0,j}} + I_1 \sum_j^{N_1} \alpha_{g_{x,y}, g_{1,j}} + \dots = f_{g_{x,y}} \quad (1.3)$$

Here  $f_{g_{x,y}}$  and  $\sigma_{g_{x,y}}$  are the pixelflux and pixel noise at the position of source  $g_{x,y}$ . Any subsample flux  $I_i$  is constant and contributes with a certain weight to the pixelflux of source  $g_{x,y}$ . If a Gaussian with width  $\sigma$  is used as a model for the beam, the value of  $\alpha_{g_{x,y}, g_{i,j}}$  is given by  $\exp(-\delta_{g_{x,y}, g_{i,j}}^2 / 2\sigma^2)$ . Here  $\delta_{g_{x,y}, g_{i,j}}$  is the distance between source  $g_{x,y}$  and  $g_{i,j}$ . Hence  $\alpha_{g_{x,y}, g_{i,j}}$  gives the contribution from source  $g_{i,j}$  to source  $g_{x,y}$ . Consequently, summing  $\alpha_{g_{x,y}, g_{i,j}}$  over all sources  $j$  in subset  $i$  gives the complete contribution of this subset to the pixelflux of source  $g_{x,y}$ .

Now the sum over all sources in subset  $x$  is taken, resulting in the following expression:

$$\sum_y^{N_x} \sigma_{g_{x,y}} + I_0 \sum_y^{N_x} \sum_j^{N_0} \alpha_{g_{x,y}, g_{0,j}} + I_1 \sum_y^{N_x} \sum_j^{N_1} \alpha_{g_{x,y}, g_{1,j}} + \dots = \sum_y^{N_x} f_{g_{x,y}} \quad (1.4)$$

It is assumed that the sum of the pixel noise values tends to zero. Previously it was discussed how summing  $\alpha_{g_{x,y}, g_{i,j}}$  over all sources  $j$  in subset  $i$  gives the contribution of subset  $i$  to one source  $g_{x,y}$  in subset  $x$ . Following this logic, it makes sense that summing that sum over all sources in subset  $x$  gives the complete contribution from subset  $i$  to the sources in subset  $x$ . This can be called the complete weighted contribution from  $i$  to  $x$ :  $W_{i,x}$ . Moreover, since  $|\delta_{g_{x,y}, g_{i,j}}| = |\delta_{g_{i,j}, g_{x,y}}|$ , the following is true:

$$W_{i,x} = \sum_y^{N_x} \sum_j^{N_i} e^{-\delta_{g_{x,y}, g_{i,j}}^2 / 2\sigma^2} = \sum_j^{N_i} \sum_y^{N_x} e^{-\delta_{g_{i,j}, g_{x,y}}^2 / 2\sigma^2} = W_{x,i} \quad (1.5)$$

Now equation 1.4 can be written more simply:

$$I_0 W_{0,x} + I_1 W_{1,x} + \dots = \sum_y^{N_x} f_{g_{x,y}} = F_x \quad (1.6)$$

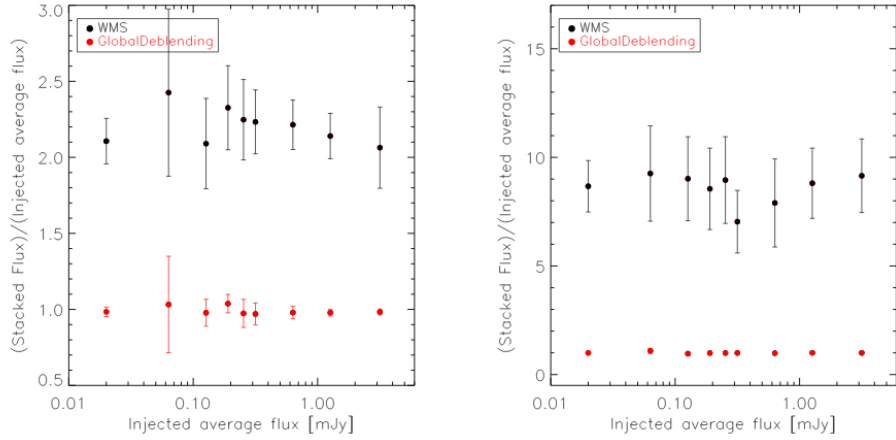


**Figure 1.5:** Simulated stacking results as a function of the average flux of stacked sources. For the simulation 1000 target sources and 2000 non-target sources have been injected into a map with a flat 0.2 mJy/beam noise level. Two different stacking methods are compared, weighted mean stacking (WMS) (black dots) and global deblending (red dots). The right panel shows the effect of increased clustering of the target sources. Adapted from Avendano (2015) (figure 4.16).

If this is done for all  $M$  subsets, the result is a linear system of  $M + 1$  equations with  $M + 1$  variables. This can be expressed as a matrix equation:

$$\begin{pmatrix} W_{1,1} & W_{1,2} & \cdots & W_{1,M} \\ W_{2,1} & W_{2,2} & \cdots & W_{2,M} \\ \vdots & \vdots & \ddots & \vdots \\ W_{M,1} & W_{M,2} & \cdots & W_{M,M} \end{pmatrix} \begin{bmatrix} I_1 \\ I_2 \\ \vdots \\ I_M \end{bmatrix} = \begin{bmatrix} F_1 \\ F_2 \\ \vdots \\ F_M \end{bmatrix} \quad (1.7)$$

The matrix in equation 1.7 is a symmetric matrix (see equation 1.5), hence a solution for this system of equations can always be found. Additionally, this property makes computation of the matrix much faster by almost a factor two.

Performance of the global deblending method has been investigated using simulations by both Kurczynski & Gawiser (2010) and Avendano (2015). They find that global deblending consistently outperforms other stacking methods like the weighted mean stacking described in the previous section. See for example figure 1.5.

#### MENTION IMPORTANCE OF COMPLETE CATALOG

Avendano (2015) finds that increased clustering of sources and higher source densities decrease the performance of weighted mean stacking,

while the global deblending method consistently gives a good approximation of the average flux of the target sources. The same is found by Kurczynski & Gawiser (2010).

## 1.5 Molecular gas mass from continuum observations

This section is based on the work of Scoville et al. (2014) and an improved analysis of the same method described in Scoville et al. (2016). The intention of both articles is to describe a method to measure the molecular gas mass of galaxies using continuum observations. An important advantage of such a method is the fact that a continuum detection of a galaxy using ALMA is observationally much less expensive than using other methods to observe molecular gas. Conventional methods such as observing the CO(1-0) transition line often take an hour or longer with ALMA, in stark contrast to a continuum detection which can be achieved in minutes. A brief overview of the reasoning behind the method will be described in this section, but both articles can be consulted for more details.

One of the foundations of this method is the observation that the emission from galaxies at submillimeter wavelengths is dominated by dust, which re-radiates the energy from stars and AGNs. Moreover, the long wavelength Rayleigh Jeans (RJ) tail is often optically thin. Because of that all dust contributes to the luminosity and consequently, the luminosity becomes a measure of the total amount of dust.

Since dust and the ISM are intimately linked, it is possible to relate dust to the ISM. However, in order for this to be possible, several conversion factors need to be known. Firstly to determine the total dust mass from the submillimeter luminosity, the dust opacity coefficient and mean temperature need to be known. Secondly, the dust-to-gas ratio is needed to convert the dust mass to ISM mass.

Because these conversion factors are difficult to determine observationally, Scoville et al. (2014) and Scoville et al. (2016) attempt to combine both into one quantity  $\alpha_{850\mu m} = L_{850\mu m} / M_{mol}$ . This quantity is empirically calibrated on a varied sample of galaxies containing 30 local star forming galaxies, 12 low-z ULIRGs and 30 z~2 SMGs (some of which appear strongly lensed).

The molecular mass for the calibration is obtained from observations of the CO(1-0) transition. A linear relation between the luminosity from this line and the 850 $\mu$ m emission is observed for all galaxy samples, see the left

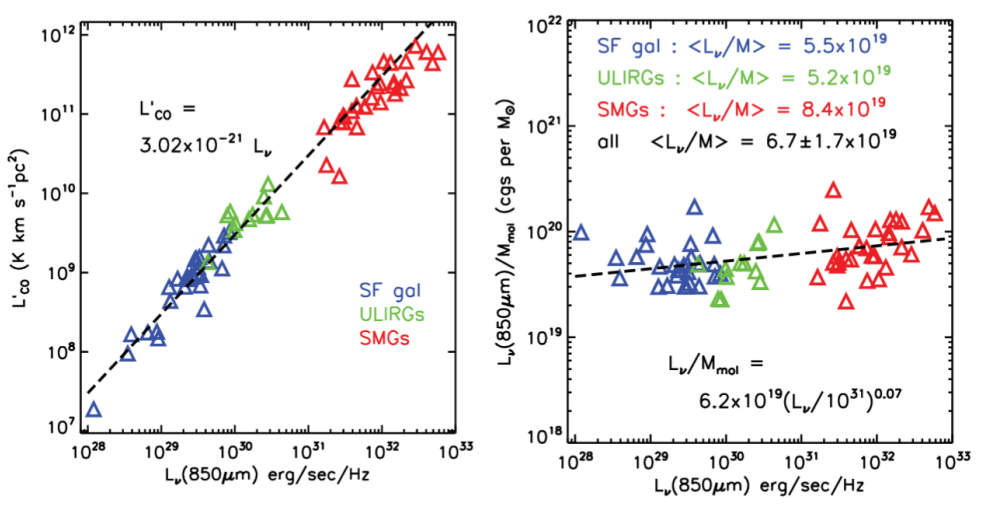


**Figure 1.6:** Left panel: CO(1-0) luminosity versus 850\$\mu\text{m}\$ luminosity. Right panel: \$L\_{850\mu\text{m}} / M\_\text{mol}\$ versus 850\$\mu\text{m}\$ luminosity. Colors represent different samples of galaxies. Adapted from Scoville et al. (2016) (figure 1).

hand side of figure 1.6. To convert from CO(1-0) luminosity to molecular gas mass, a single CO-to-H<sub>2</sub> conversion factor is utilized.

In the right hand side of figure 1.6 the value of the combined conversion factor \$\alpha\_{850\mu\text{m}}\$ is shown for different 850\$\mu\text{m}\$ luminosities. A constant calibration factor \$\alpha\_{850\mu\text{m}} = 6.7 \pm 1.7 \cdot 10^{19} \text{ erg s}^{-1} \text{ Hz}^{-1} M\_\odot^{-1}\$ for all samples of galaxies is consistent with the data (Scoville et al. 2016).

With this constant conversion factor it is possible to derive a simple equation to calculate the gas mass of galaxies from their submillimeter flux. For this purpose, the submillimeter flux needs to be converted to a rest-frame luminosity at 850\$\mu\text{m}\$. This requires a correction for luminosity distance and a conversion from different frequencies back to 850\$\mu\text{m}\$ because of redshift and different instrumental wavelengths.

For this correction from different observed frequencies to 850\$\mu\text{m}\$, the dust temperature and the spectral index of the dust opacity in the RJ regime are needed. These are taken to be constant with values \$\langle T\_{dust} \rangle\_M = 25 \text{ K}\$ for the mass weighted dust temperature and \$\beta = 1.8\$ for spectral index.

These corrections result in the following equation:

$$M_{\text{mol}} = 1.78 \cdot S_{\nu_{\text{obs}}} [\text{mJy}] \cdot (1+z)^{-4.8} \cdot \left( \frac{\nu_{850\mu\text{m}}}{\nu_{\text{obs}}} \right)^{3.8} \cdot (d_L [\text{Gpc}])^2 \cdot \left( \frac{6.7 \cdot 10^{19}}{\alpha_{850\mu\text{m}}} \right) \frac{\Gamma_0}{\Gamma_{RJ}} \cdot 10^{10} M_\odot \quad (1.8)$$

Here  $S_{\nu_{obs}}$  is the observed flux at the observing frequency,  $d_L$  is the luminosity distance and the  $\Gamma_0$  and  $\Gamma_{RJ}$  terms are corrections for the departure from the RJ law:

$$\Gamma_{RJ}(T_d, \nu_{obs}, z) = \frac{h\nu_{obs}(1+z)/kT_d}{e^{h\nu_{obs}(1+z)/kT_d} - 1} \quad (1.9)$$

And  $\Gamma_0 = \Gamma_{RJ}(25K, 850\mu m, z=0) \sim 0.7$ . Note that equation 1.8 is only applicable when the continuum observations probe the rest-frame RJ regime. Observations at too high rest-frame frequencies are not safely on the RJ tail, resulting in uncertainties in the RJ departure correction. Moreover, these high rest-frame frequencies are not necessarily optically thin. Scoville et al. (2016) advise a minimum rest frame wavelength of  $\lambda_{rest} \gtrsim 250\mu m$ . This estimate is based on a dust temperature of 25K of which the peak of the black body curve lies at , colder dust temperatures would place more stringent constraints on the redshift range.

In addition to limitations on rest-frame wavelengths, Scoville et al. (2014) and Scoville et al. (2016) limited their analysis only to high stellar mass objects  $M_* > 5 \cdot 10^{10} M_\odot$ . Lower mass systems are expected to have lower metallicities. For the same amount of dust in a low mass system, there is much more gas, the dust-to-gas ratio is lower. As a result of that, calibrating this continuum to molecular gas law for low mass galaxies will be difficult. Moreover, because of the different dust-to-gas ratio, the law might not hold at all.

## 1.6 This research

This research focusses on using stacking analyses to look at the fluxes of color selected galaxies in chapter 2 and galaxies selected by physical properties in chapter 3. The main purpose of chapter 2 is to demonstrate the effectiveness of the used stacking methods and to confirm results from previous studies. Chapter 3 uses these same stacking methods on galaxies that have been selected based on their physical properties. The stacked fluxes are used to calculate a molecular gas mass and subsequently the gas fraction of the stacked galaxies. Finally, chapter 4 concludes the report with an overall conclusion and an outlook on future work.

Throughout the report a standard  $\Lambda$ CDM cosmology is assumed, with  $H_0=70$  km/s/Mpc,  $\Omega_m=0.3$  and  $\Omega_\Lambda=0.7$  (broadly consistent with Planck Collaboration et al. (2016)).



# Chapter 2

## Color selected galaxies

This chapter is concerned with the stacking of galaxies selected based on their optical and near infra-red (NIR) colors as described in the introduction. However, the results presented in this chapter only contain a small amount of original work. Most of the chapter is concerned with the reproduction of previously published work (Greve et al. 2010; Decarli et al. 2014; Lindroos et al. 2016). This is done in order to demonstrate that the utilized stacking methods are implemented correctly and to confirm the results found by these previous studies.

### 2.1 Previous work

There is a lot of work on stacking on color selected galaxies in submillimeter observations. The focus in this section will be on three studies which study color selected galaxies in the Extended Chandra Deep Field South (ECDFS). The ECDFS is a  $0.5 \times 0.5$  deg field centered on the Hubble ultra deep field south (UDF-S). All studies utilize the Wide Multi-wavelength Survey by Yale-Chile (MUSYC), a deep survey that covers the *UBVRIzJHK* optical-NIR photometric bands.

Greve et al. (2010) use the LABOCA ECDFS Submillimeter Survey (LESS) at  $870 \mu\text{m}$  to study the submillimeter properties of color selected galaxies. Because of the low resolution of this survey, a deblending algorithm is used. This deblending algorithm not only takes neighbouring sources into account but also neighbours of neighbours. For this deblending method they consider all  $K_{\text{Vega}} \leq 20$  sources\*, sources with  $K_{\text{Vega}} > 20$  were not

---

\*the  $K_{\text{Vega}} \leq 20$  selection contains galaxies with a magnitude  $K_{\text{Vega}} \leq 20$  using a color cut to exclude stars from this sample. The exact definition is given in the next section.

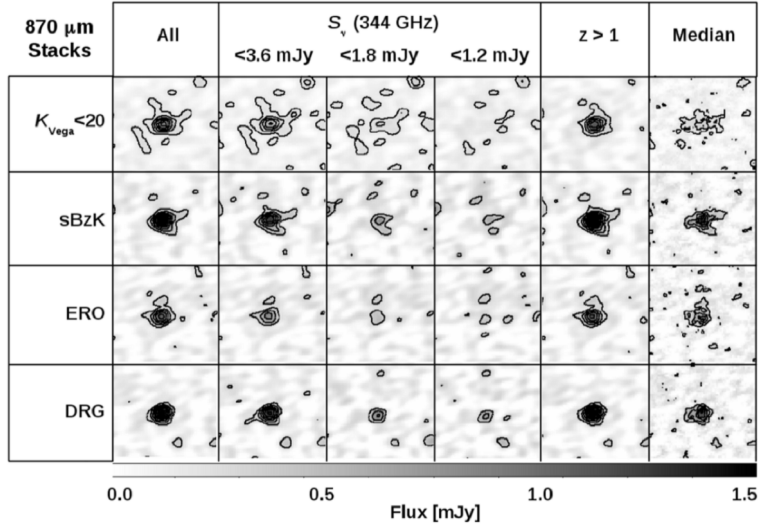


**Figure 2.1:** Stacked images of all galaxy samples considered by Decarli et al. (2014). The sizes of the stacks are 10x10 arcseconds. Greyscales are fixed for all images and contours correspond to intervals of  $2\sigma$ . All stacks use a weighted mean stacking method except the last column, which used the median. The meaning of the different selections will be explained in a later section. Adapted from Decarli et al. (2014).

considered for deblending. However, Greve et al. (2010) find that these sources do make a contribution to the stacked fluxes, with a magnitude of about  $\sim 0.065$  mJy. This offset is subsequently subtracted from their results.

Using the ALMA Cycle 0 survey (ALESS, Hodge et al. (2013)) of the 126 brightest sources of the LESS survey, Decarli et al. (2014) perform a similar stacking analysis as Greve et al. (2010). However, the interferometric ALMA data has slightly better sensitivity per beam, but more importantly a resolution  $\sim 200$  times better than the LABOCA beam (by area). Because of that, source blending is not an issue. This greatly simplifies a stacking analysis, at the expense of a much smaller sky coverage and thus lower source counts for the color selected galaxy samples. The main stacking results of Decarli et al. (2014) are shown in figure 2.1.

Another study looking at color selected galaxies using the ALESS data has been performed by Lindroos et al. (2016). This study uses a *uv*-stacking routine instead of conventional image plane stacking techniques. They confirm the fluxes found by Decarli et al. (2014) and use model fitting on the stacks in the *uv*-domain to measure the sizes of the stacked marginally resolved sources.

In the following sections, using the ALMA Cycle 0 ALESS data, the results of Decarli et al. (2014) are reproduced to confirm the correct implementation of a weighted mean stacking routine. Moreover, using image plane fitting, an attempt is made to measure the sizes of the stacked galaxies. These are compared to the results obtained Lindroos et al. (2016). This analysis is also performed on ALMA Cycle 1 data which has a higher resolution and better sensitivity. The sky coverage of this dataset data is however nearly an order of magnitude smaller than the ALESS data. Finally, the global deblending method is used to stack on color selected galaxies in the LESS survey. The results of that analysis are subsequently compared with the results from Greve et al. (2010) to test the effectiveness of the global deblending method.

## 2.2 Method

### 2.2.1 Submillimeter datasets

As described above, three submillimeter datasets were used. All datasets are observed at  $870\mu\text{m}$  and are centred on the ECDFS. These datasets will be discussed in this subsection starting with the LESS survey, the ALESS survey and finally the Cycle 1 follow-up of 15 ALESS sources.

#### LESS

The LESS survey covers the complete ECDFS ( $0.5 \times 0.5$  deg), which is the largest area of the used datasets. This survey had an integration time of over 200 hours taken on the Atacama Pathfinder EXperiment (APEX) with the Large Apex BOlometer CAmera (LABOCA). The survey is discussed in detail in Weiß et al. (2009). As mentioned above, the observation wavelength is  $870\mu\text{m}$  or 345 GHz with a passband of  $\sim 60$  GHz. The measured angular resolution of the survey is 19.2 arcseconds (FWHM) and the average rms across the entire field is 1.2 mJy/beam.

#### ALESS

The ALESS survey is a follow-up of the 126 individually detected sources in the LESS survey (Hodge et al. 2013). This survey was an early science program on ALMA, when not all antennae were on-line. The central wavelength of the survey is  $870\mu\text{m}$  or 345 GHz with a bandwidth of 8 GHz, of which  $\sim 7.5$  GHz was used after flagging. The longest used

baselines were about 125m, resulting in an average resolution of  $\sim 1.6 \times 1.15$  arcseconds (FWHM). The FWHM of the primary beam is 17.3 arcseconds, consequently, a complete ALESS field is about the same size as the LESS beam. Moreover, because of this limited field of view only a small part of the complete ECDFS is observed.

As a part of the data reduction, the data were cleaned down to a  $3\sigma$  level using CASA. Despite the short exposure times of  $\sim 2$  minutes, the typical central rms of the final maps is  $\sim 0.4$  mJy/beam.

Of the 126 target sources 122 were observed. 88 of these fields are *good quality* fields, having a central noise  $< 0.6$  mJy/beam and an axis ratio  $< 2^\dagger$ .

### ALMA Cycle 1 dataset

The final dataset is a follow-up of 15 ALESS sources as a Cycle 1 project with ALMA (Hodge et al. 2016). These observations are similar to the ALESS observations, taken at a central frequency of 345 GHz and a bandwidth of 8 GHz. The resulting primary beam has a FWHM of 17.3 arcseconds.

The targets were observed using 46 antennae with baselines up to  $\sim 1.6$  km and about 8 minutes integration on every target. After cleaning up to  $\sim 2.5\sigma$ , the synthesised beam of the maps is typically  $0.17 \times 0.15$  arcseconds for natural weighting. The typical central RMS noise is  $\sim 0.064$  mJy/beam.

#### 2.2.2 Catalog and color selection

As mentioned above, all studies use the Wide Multi-wavelength Survey by Yale-Chile (MUSYC) (Taylor et al. 2009). The catalog contains 16,910  $K$ -band selected sources. Many of these sources have an extensive wavelength coverage and are detected in all observed photometric bands ( $UBVRIzJHK$ ). At  $K_{ab} = 22$  the catalog is 100% complete for point sources and 96% complete for extended sources with a scale radius of  $\sim 0.5$  arcseconds. Before calculating the magnitude in any particular band from the catalog, a flux-aperture correction must be applied. This correction is derived from the  $K$ -band imaging (Taylor et al. 2009).

Simpson et al. (2014) used SED fitting to determine the photometric redshift of a large number of sources in the catalog. Additionally, the catalog contains the spectroscopic redshifts of limited number of sources

---

<sup>$\dagger$</sup> From figure 1 in Hodge et al. (2013) it can be noted that only requiring axis ratio  $< 2$  is a sufficient criterion to select all good quality fields.

from various studies. Comparing the spectroscopic redshifts with the photometrically determined redshifts gives  $\Delta z/(1+z) \sim 0.011$  (Decarli et al. 2014). For the redshift selection used for this project the photometric redshift estimate is used unless a spectroscopic redshift is available for any particular source.

For the color selection of galaxies, several criteria are used, as described in the introduction. For this report four selections are made. The first and most significant one is the  $K_{Vega} < 20$  (Greve et al. 2010). This is not a true color selection, but rather it ensures completeness of the sample up to the limiting Vega magnitude. Also, this magnitude cutoff has been used by previous studies, facilitating a comparison with these works. Moreover, in addition to this  $K$ -band magnitude cutoff, stars are excluded from the sample using a color-color selection. Because of the properties of the  $K_{Vega} < 20$  selection described above, all color selected galaxies must be part of this  $K_{Vega} < 20$  sample. The exact definitions of the used color selections are given below.

- The  $K_{Vega} < 20$  sample contains galaxies with  $K_{Vega} < 20$  or in AB magnitudes:  $K_{AB} < 21.83$ , using the same VEGA-AB offset as utilized by Decarli et al. (2014). Greve et al. (2010) uses  $K_{AB} < 21.9$  instead. The distinction between galaxies and stars is achieved by requiring  $(z - K - 0.04) > 0.3 \cdot (B - z + 0.56) - 0.5$
- sBzK galaxies, in addition to belonging to the  $K_{Vega} < 20$  sample, require the following color selection  $(z - K - 0.04) - (B - z + 0.56) > -0.2$ .
- EROs are objects with  $(R - K) > 3.35$  and  $(J - K) > 0.1$ .
- Galaxies belonging to the DRG sample require  $(J - K) > 1.32$

In addition to the fact that sBzK, ERO and DRG galaxies must be part of the  $K_{Vega} < 20$  sample, there is considerable overlap between these color selections. Greve et al. (2010) give a detailed description of this overlap.

### 2.2.3 Stacking methods

#### ALMA

Different stacking methods are used for the different datasets. Because of the high resolution of the ALMA datasets, source blending is not an issue. As a result of that, a simple weighted mean stacking method can

be utilized. An identical stacking analysis is used for both the Cycle 0 and Cycle 1 data.

The ALMA observations are, as described in a previous section, limited in size and do not cover the complete ECDFS. The primary beam has a FWHM of 17.3 arcseconds. Following Decarli et al. (2014), only sources within 1.2 times the primary beam are used in the stacking analysis.

For the stacking, a small 10x10 arcseconds cutout is made around every target source. This cutout is corrected for primary beam attenuation. Specifically, by assuming a Gaussian beam, the following correction is appropriate:

$$F_{corr} = e^{\frac{\Delta^2 - 4\ln 2}{\Theta^2}} \quad (2.1)$$

Here  $\Theta$  is the FWHM of the primary beam and  $\Delta$  is the distance from the stacking target source to the pointing center. Using the center of a cutout, a primary beam correction is calculated, this value is subsequently applied to all pixels in the cutout.

Following Decarli et al. (2014), the weights used for the stacking analysis are derived from the primary beam correction:  $w_{target} = 1/F_{corr}^2$ . This method is based on the assumption that noise increases proportionally to the primary beam correction. More importantly, when considering multiple observations, it relies on the fact that the central noise of every field is roughly the same. Because this analysis is limited to the *good-quality* ALMA fields, these assumptions are reasonable.

To measure the flux in a stacked image, Decarli et al. (2014) measure the peak flux within a radius of 3 arcseconds of the center of the stacked image. This is done in order to account for small errors in the astrometry of the ALMA observations and the catalog. Staying in line with Decarli et al. (2014), the error on this flux is estimated using a Monte Carlo method. For every field where  $N$  target source cutouts are made,  $N$  additional cutouts at random positions are taken. These cutouts at random positions are stacked in the same way as the target cutouts. This is repeated 50 times and the variance of the fluxes obtained by the random stacks is used as an estimate of the error of the flux.

Bootstrapping is also a possible method to get insight into the error on the flux. This is easily implemented by drawing a random sample from the target cutouts with replacement and stacking on this random selection. However it should be noted that this not only measures the instrumental error, but also includes the sample variance. Because of that, errors derived through bootstrapping are larger than errors obtained with the Monte Carlo method described above.

## LESS

Because of the low resolution of the LESS data, blending of sources is an issue. As described in the introduction, applying a weighted mean stacking method to this kind of data will likely give incorrect results. Consequently, a more sophisticated stacking analysis is necessary. The global deblending method described is a suitable method for this kind of data. The implementation of this method will be outlined below.

Since there is a substantial overlap between the different color selected galaxy samples, it is not possible to solve for the flux of all samples at the same time. Therefore every color selected sample of galaxies is treated individually.

For example, looking only at sBzK galaxies, this results in the following system of equations when referring to equation 1.7:

$$\begin{pmatrix} W_{not,sBzK} & W_{not,not} \\ W_{sBzK,sBzK} & W_{sBzK,not} \end{pmatrix} \begin{bmatrix} I_{not} \\ I_{sBzK} \end{bmatrix} = \begin{bmatrix} F_{not} \\ F_{sBzK} \end{bmatrix} \quad (2.2)$$

Where the subscripts refer to sources which are part of the sBzK sample or not. Solving this system gives  $I_{sBzK}$ , which is the stacked and deblended submillimeter flux of the sample. This analysis is repeated for every sample to obtain the stacked and deblended fluxes for those samples.

To estimate the error of the stacked deblended flux, a similar method as the ALMA stacking is used. For every target source, at a random position in the neighbourhood of that source a random flux is measured. These random fluxes are summed and solved for in the same way as the target fluxes. This is repeated 100 times and the variance of these stacked deblended random fluxes is used as a measure of the error.

### 2.2.4 Size measurement

Using the stacking method described above for the ALMA datasets, stacked images of 10x10 arcseconds are obtained. The pixels of these stacked images are then binned as a function of radius around the center of the stacked image. The value of the flux in each radial bin is determined from the median of the fluxes of the pixels in the bin. The variance of these fluxes is taken to be the error of that flux.

Using these binned fluxes as a function of radius, a Gaussian is fitted:

$$\alpha e^{-r^2 \frac{4\ln 2}{\Theta^2}} \quad (2.3)$$

Where  $\Theta$  is the fitted FWHM of the flux distribution and  $\alpha$  the amplitude.

The fitted FWHM is more spread out than the actual flux distribution of the source, because it has been convolved with the synthesised beam of the observations. It is not unreasonable to approximate both the source and the synthesised beam can with a Gaussian. Then, it can be shown, using the fourier transform theorem for convolutions, that the convolution of two Gaussians with a FWHM of  $\Theta_{source}$  and  $\Theta_{beam}$  results in another another Gaussian with a FWHM of  $\Theta = \sqrt{\Theta_{source}^2 + \Theta_{beam}^2}$ . This gives a very simple way to deconvolve the observation without resulting to sometimes rather messy numerical deconvolution methods.

A complication for this method is the fact that not every observation in the stack has the same synthesised beam. It is not trivial to determine what the correct value to use for deconvolution is. For this project, the weighted average of the major axis of the synthesised beams corresponding to the individual cutouts is used. The weights are taken to be the same as the weights used for the stacking analysis. This method is motivated by the random orientation of the synthesised beam of every cutout in the stacked image.

Assuming a unit amplitude for the beam at its center, a simple expression for the integrated flux of the Gaussian source can be obtained.

$$\alpha \frac{\Theta}{\Theta_{beam}} \quad (2.4)$$

Where  $\Theta$  is the fitted FWHM,  $\alpha$  the amplitude of that fit (both from equation 2.3) and  $\Theta_{beam}$  the FWHM of the beam of the stacked image.

The error on the fitted values is obtained through bootstrapping by drawing a random sample from the target cutouts with replacement and stacking on this random selection. Using the same method as the regular stacks, a Gaussian is fitted to measure the deconvolved size of the stacked source. This is repeated for 500 cycles, where the variance of the sizes determined that way is taken as an measure of the error.

Sub-sample	N.gal	This work Flux(mJy)	Greve et al. (2010)	N.gal Flux(mJy)
<i>All galaxies</i>				
$K_{Vega} < 20$	8492	$0.18 \pm 0.01$	$0.20 \pm 0.01$	8266
sBzK	823	$0.48 \pm 0.06$	$0.48 \pm 0.04$	744
ERO	1222	$0.41 \pm 0.04$	$0.42 \pm 0.03$	1253
DRG	770	$0.42 \pm 0.05$	$0.41 \pm 0.04$	737

**Table 2.1:** Results of the stacking analysis using the global deblending method and the LESS survey. Also shown are the results from Greve et al. (2010) which preformed a similar analysis of the same data.

## 2.3 Results

### 2.3.1 LESS

This section presents the results of a stacking analysis on color selected galaxies in the LESS survey. These results are compared to are compared to the findings of Greve et al. (2010). The main difference is the stacking and deblending method in both studies. Greve et al. (2010) uses a neighbours of neighbours deblending and stacking method and this work uses the global deblending method. The stacking analysis applied to the whole sample of color selected galaxies galaxies, the stacked fluxes can be found in table 2.1.

### 2.3.2 ALMA

#### All galaxies

The results obtained in this section use the same method and dataset (Hodge et al. 2013) as Decarli et al. (2014) and can be found in table 2.2. The results for stacking on the whole sample of color selected galaxies are shown, in addition to the results of using the median instead of a weighted average on that same sample.

In an attempt to account for biases Decarli et al. (2014) exclude bright sources from the stacking. The first group excludes sources that have a 344 GHz flux higher than 3.6 mJy in the ALMA observations. Sources with this flux were individually detected in the original LESS survey. The subsequent lower cutoff is 1.8 mJy, this cutoff is appropriate when a individually detected LESS source actually consists of two individual sources. The

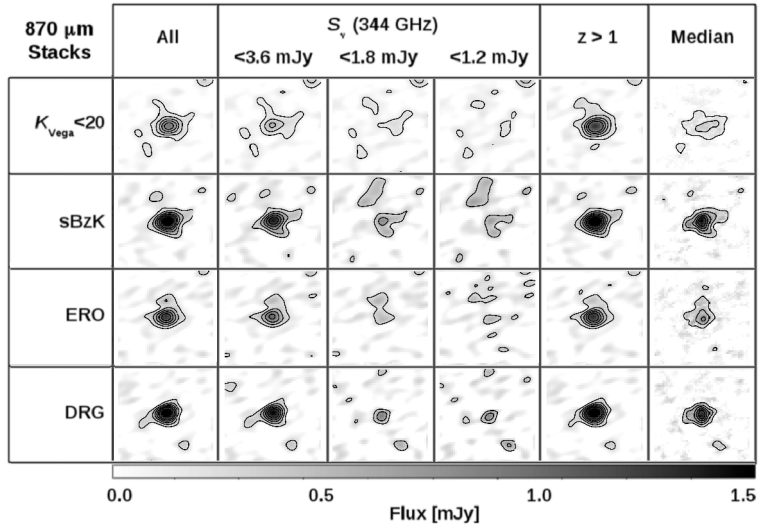


**Figure 2.2:** Stacked images of all galaxy samples. The sizes of the cutouts are 10x10 arcseconds. Greyscales are fixed for all images and contours correspond to intervals of  $2\sigma$ . All stacks use a weighted mean stacking method except the last column, which used the median. The different columns refer to different selection criteria as described in the text.

last cutoff equals the  $\sim 3\sigma$  limit of the ALMA observations. Individually detected ALESS sources are excluded from the stack for this last group. The these results of these flux cutoffs are likewise reported in table 2.2.

### Z>1 galaxies

Color selected galaxies at a redshift of 1.0 or higher in the ALESS dataset have been studied by both Decarli et al. (2014) and Lindroos et al. (2016). Using the same method as the previous section, this work also performs the same stacking analysis. The results and a comparison to the two studies mentioned above are shown in table 2.3.

The stacked images of all selections from tables 2.2 and 2.3 can be found in figure 2.2. This figure has exactly the same setup as figure 2.1 with a fixed greyscale from 0 mJy to 1.5 mJy and countours with a spacing of  $2\sigma$ .

### ALMA Cycle 1

Due to the limited sky coverage of the ALMA cycle 1 observations, only as small number of color selected galaxies are available for stacking analysis. These results are shown in table 2.4.

Sub-sample	N.gal	This work Flux(mJy)	Decarli et al. (2014) Flux(mJy)
<i>All galaxies</i>			
$K_{Vega} < 20$	103	$0.80 \pm 0.06$	$0.78 \pm 0.06$
sBzK	22	$1.98 \pm 0.10$	$1.88 \pm 0.11$
ERO	26	$1.18 \pm 0.09$	$1.11 \pm 0.10$
DRG	20	$1.82 \pm 0.10$	$1.77 \pm 0.12$
<i>Median All galaxies</i>			
$K_{Vega} < 20$	103	$0.36 \pm 0.05$	$0.34 \pm 0.06$
sBzK	22	$1.53 \pm 0.10$	$1.48 \pm 0.13$
ERO	26	$0.72 \pm 0.10$	$0.89 \pm 0.10$
DRG	20	$1.39 \pm 0.10$	$1.47 \pm 0.13$
$S_\nu(344\text{GHz}) < 3.6 \text{ mJy}$			
$K_{Vega} < 20$	97	$0.44 \pm 0.06$	$0.53 \pm 0.05$
sBzK	20	$1.35 \pm 0.10$	$1.31 \pm 0.11$
ERO	25	$0.88 \pm 0.09$	$0.82 \pm 0.12$
DRG	19	$1.47 \pm 0.10$	$1.41 \pm 0.11$
$S_\nu(344\text{GHz}) < 1.8 \text{ mJy}$			
$K_{Vega} < 20$	90	$0.21 \pm 0.06$	$0.23 \pm 0.05$
sBzK	15	$0.68 \pm 0.12$	$0.77 \pm 0.14$
ERO	21	$0.44 \pm 0.10$	$0.45 \pm 0.13$
DRG	13	$0.73 \pm 0.11$	$0.89 \pm 0.14$
$S_\nu(344\text{GHz}) < 1.2 \text{ mJy}$			
$K_{Vega} < 20$	79	$0.20 \pm 0.07$	$0.20 \pm 0.08$
sBzK	13	$0.57 \pm 0.14$	$0.60 \pm 0.17$
ERO	17	$0.43 \pm 0.11$	$0.39 \pm 0.13$
DRG	12	$0.69 \pm 0.11$	$0.68 \pm 0.15$

**Table 2.2:** Results of the stacking analysis of the ALESS survey. Both the flux derived in this work and the Decarli et al. (2014) flux have been obtained using the same method.

Sub-sample	N.gal	This work Flux(mJy)	Decarli et al. (2014) Flux(mJy)	Lindroos et al. (2016) Flux(mJy)
<i>redshift &gt;1</i>				
$z K_{Vega} < 20$	51	$1.19 \pm 0.07$	$1.16 \pm 0.09$	$1.14 \pm 0.07$
sBzK	21	$2.05 \pm 0.10$	$1.89 \pm 0.10$	$1.83 \pm 0.10$
ERO	25	$1.24 \pm 0.09$	$1.15 \pm 0.11$	$1.12 \pm 0.10$
DRG	19	$1.97 \pm 0.10$	$1.90 \pm 0.13$	$1.89 \pm 0.11$

**Table 2.3:** Results of the stacking analysis using the global deblending method and the LESS survey. Also shown are the results from Greve et al. (2010) which preformed a similar analysis of the same data.

Sub-sample	N.gal	Cycle 1 Flux(mJy)	Decarli Flux(mJy)
<i>All</i>			
K-selected	13	$0.42 \pm 0.22$	$0.78 \pm 0.06$
sBzK	3	$1.14 \pm 0.35$	$1.88 \pm 0.11$
ERO	2	$0.22 \pm 0.04$	$1.11 \pm 0.10$
DRG	1	$1.01 \pm 0.01$	$1.77 \pm 0.12$
<i>redshift &gt;1</i>			
K-selected	6	$0.66 \pm 0.18$	$1.16 \pm 0.09$
sBzK	3	$1.14 \pm 0.72$	$1.89 \pm 0.10$
ERO	2	$0.22 \pm 0.04$	$1.15 \pm 0.11$
DRG	1	$1.01 \pm 0.01$	$1.90 \pm 0.13$
<i>Median(All)</i>			
K-selected	13	$0.14 \pm 0.07$	$0.78 \pm 0.06$
sBzK	3	$0.28 \pm 0.93$	$1.88 \pm 0.11$
ERO	2	$0.22 \pm 0.05$	$1.11 \pm 0.10$
DRG	1	$1.01 \pm 0.01$	$1.77 \pm 0.12$

**Table 2.4:** Results of the stacking analysis of the cycle 1 observations. As a reference the results from Decarli et al. (2014) are shown also.

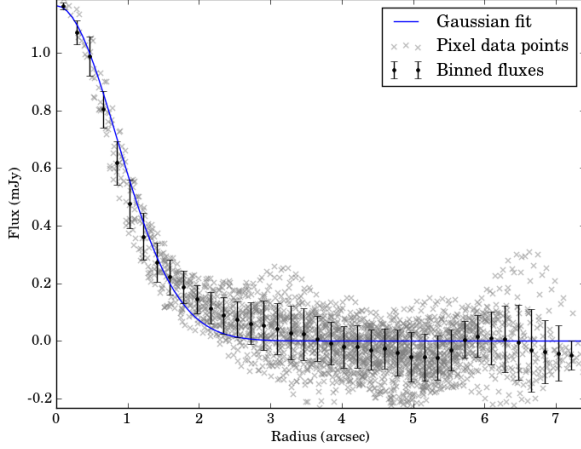


**Figure 2.3:** Stacked flux of  $K_{\text{Vega}} < 20$  galaxies with  $z > 1.0$  as a function of radius from the center of the cutout. Grey crosses show the flux of individual pixels while black dots show the median of the radially binned fluxes. The error on the binned fluxes is derived from the variance of the pixel fluxes in that bin. The gaussian fit is shown in blue.

### Sizes of stacked galaxies

Lindroos et al. (2016) et al measure the sizes of stacked galaxies in addition to the flux with a *uv*-stacking routine. This work uses image stacking and the Gaussian fitting method described in a previous section to measure the sizes of stacked galaxies from the ALESS survey. An example such a fit is shown in figure 2.3. The sizes obtained this way can be found in table 2.5, the sizes measured by Lindroos et al. (2016) are also shown. The integrated Gaussian fluxes derived by this work are calculated using equation 2.4 and can also be found in table 2.5.

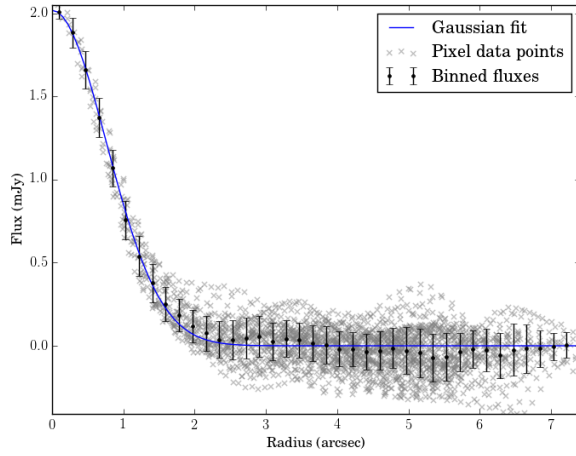


**Figure 2.4:** Stacked flux of sBzK galaxies with  $z > 1.0$  as a function of radius from the center of the cutout. Grey crosses show the flux of individual pixels while black dots show the median of the radially binned fluxes. The error on the binned fluxes is derived from the variance of the pixel fluxes in that bin. The gaussian fit is shown in blue.

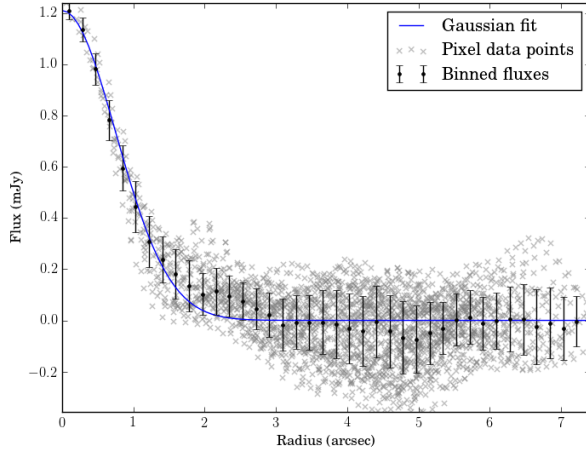


**Figure 2.5:** Stacked flux of ERO galaxies with  $z > 1.0$  as a function of radius from the center of the cutout. Grey crosses show the flux of individual pixels while black dots show the median of the radially binned fluxes. The error on the binned fluxes is derived from the variance of the pixel fluxes in that bin. The gaussian fit is shown in blue.

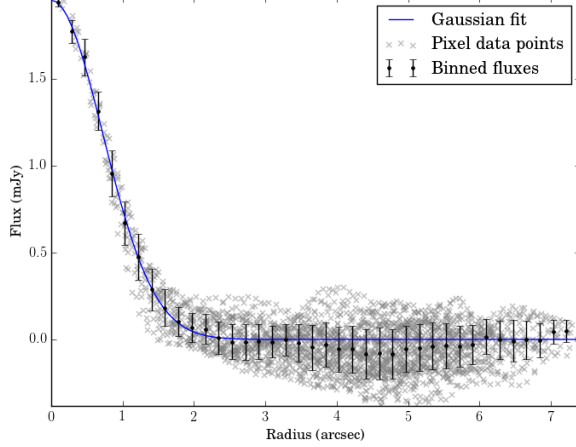


**Figure 2.6:** Stacked flux of DRG galaxies with  $z > 1.0$  as a function of radius from the center of the cutout. Grey crosses show the flux of individual pixels while black dots show the median of the radially binned fluxes. The error on the binned fluxes is derived from the variance of the pixel fluxes in that bin. The gaussian fit is shown in blue.

Sub-sample	N.gal	FWHM (arcsec)	Lindroos FWHM (arcsec)	Gaussian Flux (mJy)	Lindroos Gaussian Flux(mJy)
<i>All</i>					
$K_{Vega} < 20$	51	$1.32 \pm 0.35$	$0.73 \pm 0.14$	$1.55 \pm 0.42$	$1.85 \pm 0.30$
sBzK	21	$0.91 \pm 0.27$	$0.73 \pm 0.15$	$2.34 \pm 0.38$	$2.34 \pm 0.32$
ERO	25	$0.89 \pm 0.39$	$0.65 \pm 0.17$	$1.40 \pm 0.32$	$1.51 \pm 0.22$
DRG	19	$0.87 \pm 0.19$	$0.71 \pm 0.14$	$2.28 \pm 0.40$	$2.44 \pm 0.28$

**Table 2.5:** Results of using image stacking to estimate the size of the stacked sources as well as an estimation of the integrated gaussian flux of those sources. These results are compared to the sizes and fluxes obtained by Lindroos et al. (2016).

## 2.4 Discussion

### 2.4.1 LESS

The results from the stacking analysis on color selected galaxies in the LESS survey are summarized in table 2.1. The fluxes found in this work and the fluxes found by Greve et al. (2010) are very close. Only the flux from the  $K_{Vega} < 20$  sample found by this work is more than one standard deviation away from the value found by Greve et al. (2010), the rest are within the error-bars.

This is interesting because the fluxes derived by Greve et al. (2010) are obtained through a different deblending and stacking method than used for this analysis. Moreover, Greve et al. (2010) manually subtract a background flux of 0.065 mJy which they attribute to  $K_{Vega} > 20$  galaxies. These galaxies were not taken into account for their neighbours of neighbours deblending. The value of this background flux is derived from their stacked images, see figure 6 in Greve et al. (2010) for more details.

The global deblending method does not need any additional corrections to the flux given by the algorithm since the effect of all sources is taken into consideration. This test is a real world demonstration of the effectiveness of the global deblending method. It also demonstrates that the MUSYC catalog is complete enough to account for all submillimeter flux contributions up to the flux level of the stacking analysis.

In table 2.1 it can be seen that the number counts of galaxies used by this work and Greve et al. (2010) are slightly different ( $\sim 4\%$ ). This can be attributed to the fact that Greve et al. (2010) used a previous release of the MUSYC catalog. The small changes in the photometric calibration result in the observed differences in the numbers of color selected galaxies. Nevertheless, these differences do not seem to have effected the stacked fluxes significantly.

### 2.4.2 ALMA

#### Stacked fluxes

In this section the results from a weighted mean stacking analysis on the ALMA Cycle 0 ALESS survey and ALMA cycle 1 observations will be discussed. The results can be found in tables 2.2 and 2.3 (Cycle 0) and 2.4 (Cycle 1).

The main purpose of this stacking analysis was to confirm the correct implementation of the weighted mean stacking method outlined in De-

carli et al. (2014). This is done by verifying that the fluxes obtained in this work are the same as the fluxes obtained by Decarli et al. (2014) which used the same method and ALESS (Cycle 0) dataset.

From tables 2.2 and 2.4 it is clear that the stacked fluxes obtained in this work and the fluxes from Decarli et al. (2014) are not the same. Since the number of galaxies found in every category are the same for both this work and Decarli et al. (2014), the discrepancy must arise from the implementation of the weighted mean stacking method.

A considerable amount of effort was expended to verify every step in the stacking process, but no errors were found. Because of that, the most likely source of the discrepancy is a difference in the datasets used for the stacking analysis. This was verified by checking the meta-data of the images used for the stacking analysis. The images used for this work are from a later date, with a slightly different calibration.

Despite this difference, the vast majority of the stacked fluxes from both this work and Decarli et al. (2014) are within one standard deviation of each-other. Moreover, comparing 2.1 from Decarli et al. (2014) and figure 2.2, it is clear that the stacked sources look very similar.

The dataset used by Lindroos et al. (2016) has not been verified. However, in table 2.4 it can be seen that the fluxes obtained by their *uv*-stacking analysis are very close to the values of Decarli et al. (2014). Because of that it seems reasonable that Lindroos et al. (2016) used the same dataset as Decarli et al. (2014).

The Cycle 1 observations only cover 15 ALESS sources, so the number of color selected galaxies covered by these observations is very small. Due to these small number statistics, it is difficult to interpret the data. Moreover, when comparing the stacked fluxes obtained through the weighted mean stacking and fluxes from the median stacks, it is clear that the weighted mean fluxes are dominated by bright sources, the same is true for the ALESS Cycle 0 stacks.

### Sizes of submillimeter galaxies

Lindroos et al. (2016) uses a *uv*-stacking method to measure the sizes of color selected galaxies at redshifts  $>1$ . For this work, the same is attempted in the image plane by fitting a Gaussian to radially averaged fluxes. The results of this effort are summarized in table 2.5 and the fits can be seen in figures 2.3, 2.4, 2.5 and 2.6.

From table 2.5 it is clear that for all color selected samples, the sizes are overestimated compared to the *uv*-stacking method. Moreover, the sizes measured by this work are not within the error-bars of the sizes measured

Sub-sample	N.gal	FWHM (arcsec)	Lindroos FWHM (arcsec)	Gaussian Flux (mJy)	Lindroos Gaussian Flux(mJy)
<i>All</i>					
$K_{Vega} < 20$	51	$1.21 \pm 0.35$	$0.73 \pm 0.14$	$1.46 \pm 0.42$	$1.85 \pm 0.30$
sBzK	21	$0.73 \pm 0.27$	$0.73 \pm 0.15$	$2.21 \pm 0.38$	$2.34 \pm 0.32$
ERO	25	$0.72 \pm 0.39$	$0.65 \pm 0.17$	$1.32 \pm 0.32$	$1.51 \pm 0.22$
DRG	19	$0.71 \pm 0.19$	$0.71 \pm 0.14$	$2.15 \pm 0.40$	$2.44 \pm 0.28$

**Table 2.6:** Same as table 2.5, but the FWHM used for deconvolution has been multiplied by a constant factor 1.06.

by Lindroos et al. (2016). A possible explanation is that beam FWHM used for the deconvolution has not been correctly estimated.

The beam FWHM of a stacked image is not trivial to determine, because of the fact that the observations used for a stacked image all have different beams. At the moment the beam FWHM of the stacked image is estimated by the weighted average of the major axis of the synthesised beams of the images which are part of the stack. If this method underestimates the true FWHM of the beam of the stacked image, the overestimation of the sizes measured by this work could be explained.

For the sBzK, ERO and DRG samples, this works overestimates the sizes by a factor  $\sim 1.3$ . The discrepancy of the  $K_{Vega} < 20$  galaxies is a bit larger, but figure 2.3 indicates that a Gaussian is probably not the best way to describe this source.

If the value of the beam FWHM used for the deconvolution is multiplied by a constant factor of 1.06 for all observations, much closer to the values obtained by Lindroos et al. (2016). The results of this change are shown in table 2.6. These FWHMs are well within the error-bars from Lindroos et al. (2016), except for the  $K_{Vega} < 20$  stack.

This observation shows that the results of size measurement in the image plane are very sensitive to the assumed beam of the stacked image. Therefore, a more sophisticated method to deconvolve the stacked images might be more appropriate. Especially since the factor 1.06 is essentially a free parameter at the moment.

### 2.4.3 Overall discussion

Comparing the stacked fluxes from the LESS survey and ALMA shows that the fluxes observed by ALMA are significantly higher than the fluxes

according to LESS, this is also discussed by Decarli et al. (2014). The reason is likely the fact that the stacks are dominated by bright galaxies. This is substantiated by looking at the median and  $S_\nu(344\text{GHz}) < 1.2$  sections of table 2.2, the stacked fluxes of these cuts are much closer to the values obtained by stacking on the LESS data.

Looking at the fluxes of the color selections, it is clear that the  $K_{Vega} < 20$  galaxies have the lowest flux. This is expected because this sample is not a true color selection. It only represents a magnitude limit and a distinction from stars. The highest flux is from the sBzK galaxies, this criterion indeed seems to select for star forming galaxies which generally have higher submillimeter fluxes. The same goes for DRG galaxies, though ERO galaxies seem to be less bright in the submillimeter. This might be explained by the fact that, as mentioned in the introduction, it was found that ERO galaxies have a much lower star formation rate than sBzK galaxies.

## 2.5 Conclusion

In this chapter the global deblending method for simultaneous stacking and deblending is tested using LESS observations. It is shown that the results from this method are in good agreement with previous results, validating the effectiveness of global deblending in a real world example.

Using data from the ALESS survey, results on stacking on color selected galaxies from Decarli et al. (2014) and Lindroos et al. (2016) are reproduced. A discrepancy is found, which can be explained by the fact that different calibrations of the original dataset are used.

It is found that the number of galaxies in the Cycle 1 ALMA observations is not sufficient to perform a reliable stacking analysis.

Finally, using a Gaussian fit on azimuthally averaged image plane stacks, an attempt is made to measure the sizes of color selected galaxies. These results are compared to the results obtained by the *uv*-stacking method from Lindroos et al. (2016). It is found that the deconvolution necessary to determine the source size is very sensitive to the assumed beam FWHM of the stacked image. With the addition of one free parameter, it is possible to get very similar results as Lindroos et al. (2016).



Chapter **3**

# Gas fraction of galaxies selected by physical properties

This chapter focusses on stacking on galaxies which are selected by their physical properties, inspired by the work of Scoville et al. (2016). The stacked fluxes are converted to molecular gas masses and subsequently the gas fraction of the stacked galaxies. Comparing the gas fraction of galaxies with different stellar masses and specific star formation rates can give insight into the mechanisms behind star formation in galaxies.

## 3.1 Previous work

As described in the introduction, Scoville et al. (2014) developed a method to measure the molecular gas mass of galaxies using continuum observations. In a more recent article (Scoville et al. 2016) this method is improved and used to measure the gas masses of star forming galaxies. A brief summary of their results is given in this section, the original paper can be consulted for more details.

Scoville et al. (2016) use a sample of 145 galaxies selected to cover a broad range of star formation rates at galaxy masses  $\gtrsim 10^{10} M_{\odot}$ . These galaxies were observed as part of a ALMA Cycle 2 program where the  $\langle z \rangle = 1.15$  and  $\langle z \rangle = 2.2$  redshift bins were observed using band 7 (345 GHz) and the high redshift bin  $\langle z \rangle = 4.4$  used band 6 (240 GHz). Most of the galaxies were detected individually for the low redshift samples, but for the high redshift sample about half the galaxies were detected individually. These observations were then used for a stacking analysis. For this analysis, the galaxies were stacked in bins of stellar mass and specific star

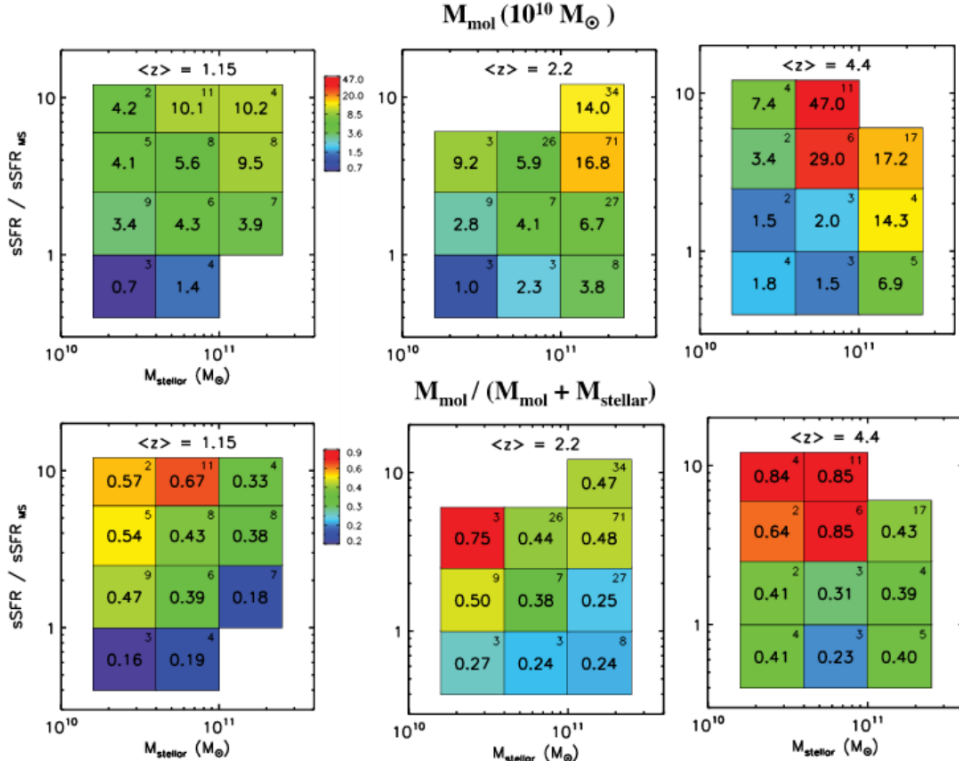


**Figure 3.1:** Top row: Gas masses derived from stacked images of galaxy subsamples in bins of stellar mass and  $sSFR_{ms}$ . The number in the upper right of the bins indicates the signal-to-noise ratio and the central number gives the gas mass (in  $10^{10} M_\odot$ ). Bottom row: Same as top row, but for the gas fraction. Adapted from Scoville et al. (2016) (figure 6).

formation rate in units of specific star formation rate of the main sequence  $sSFR/sSFR(ms) \equiv sSFR_{ms}$ .

The results of this stacking analysis are shown in figure 3.1. This figure shows that the molecular gas mass in the stellar mass and  $sSFR_{ms}$  bins increases with redshift. Additionally, bins with a higher  $sSFR_{ms}$  also have a higher gas mass. Finally, it can be observed that the gas mass of galaxies with a higher stellar mass is higher than for galaxies with lower stellar masses. The combination of these last two trends generate a gradient of increasing gas mass towards the top right of the figures.

The gas fractions, defined as  $f_{gas} = M_{mol}/(M_{mol} + M_*)$ , shows a trend where bins with a higher  $sSFR_{ms}$  and lower stellar masses have higher gas fractions. These trends result in a gradient towards the top left corner, which is especially clear for the  $\langle z \rangle = 1.15$  redshift bin. An increase in gas fraction with redshift is also observed.

Using the stacking results shown in figure 3.1 Scoville et al. (2016) fit a function to give the gas fraction in terms of stellar mass,  $sSFR_{ms}$  and redshift:

$$\frac{M_{mol}}{M_{mol} + M_*} = (0.30 \pm 0.02) \left( \frac{M_*}{10^{11} M_\odot} \right)^{-0.02 \pm 0.02} \cdot \left( \frac{1+z}{3} \right)^{0.44 \pm 0.05} \left( \frac{sSFR}{sSFR_{ms}} \right)^{0.32 \pm 0.02} \quad (3.1)$$

In the remainder of this chapter, a similar analysis will be applied to the ALESS, LESS and HerMES surveys in the ECDFS.

## 3.2 Method

### 3.2.1 Submillimeter datasets

#### ALESS and LESS

In this chapter, three submillimeter datasets will be used for stacking analysis. At  $870\mu\text{m}$  the ALESS and LESS surveys will be used. Both these surveys have been described in the previous chapter, hence the reader is referred to section 2.2.1 for more details.

#### HerMES ECDFS

As being one of the most extensively studied regions in the sky, the ECDFS has also been observed by the SPIRE instrument on the *Herschel* space telescope. The ECDFS has been observed as part of a large legacy programme called the *Herschel* Multi-tiered Extragalactic Survey (HerMES).

For this work, only SPIRE  $500\mu\text{m}$  data will be used. These observations have a relatively low resolution of  $\sim 34$  arcseconds and a  $1\sigma$  depth of  $1.9$  mJy. A complete description of the HerMES dataset can be found in Oliver et al. (2012).

### 3.2.2 Catalog

The catalog at the basis of the work described in this chapter is a result of the SIMPLE survey described by Damen et al. (2011). This survey combines deep *Spitzer* IRAC imaging with the MUSYC survey used in the previous chapter. Sources in the catalog are detected in the NIR from a  $3.6$  and  $4.5\mu\text{m}$  map.

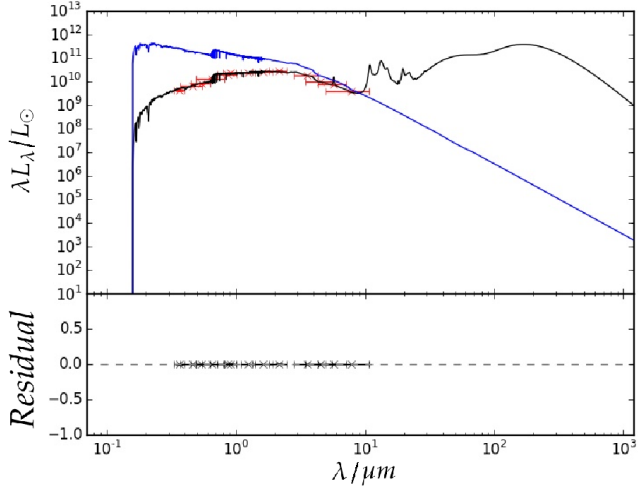


**Figure 3.2:** Example of a fitted SED. The model is shown in black and the photometric datapoints are shown in red. The blue line indicates the spectrum of the unattenuated stellar population. In the subplot shows the residual between the model and photometric fluxes.

The survey contains 61.233 sources, 19.993 of which have 13-band photometry, being detected in all photometric bands of this survey (*UBVRIzJHK*, 3.6, 4.5, 5.8 and 8.0  $\mu\text{m}$ ). Photometric and spectroscopic redshifts from Ilbert et al. (2009), Cardamone et al. (2010) and Simpson et al. (2014) are used with a preference for spectroscopic reshift or the most recent determination of a photometric redshift.

### 3.2.3 SED fitting

The fluxes provided by the catalog described in the previous section are used for SED fitting to determine the physical properties of the observed galaxies. This is done using MAGPHYS (da Cunha et al. 2008), which has been briefly described in the introduction. For this work, the high-z expansion of MAGPHYS has been used (da Cunha et al. 2015).

A source from the catalog is only fitted if it has photometry in at least 4 bands and a redshift determination. Unfortunately it is not possible to use MAGPHYS to determine the redshift of a large sample of sources at the moment.

In total 39.468 sources have been fitted with a SED, giving estimations on a large number of physical parameters for every source. The most relevant parameters for this work are the stellar mass and the star formation rate. An example of a fitted spectral energy distribution is shown in figure

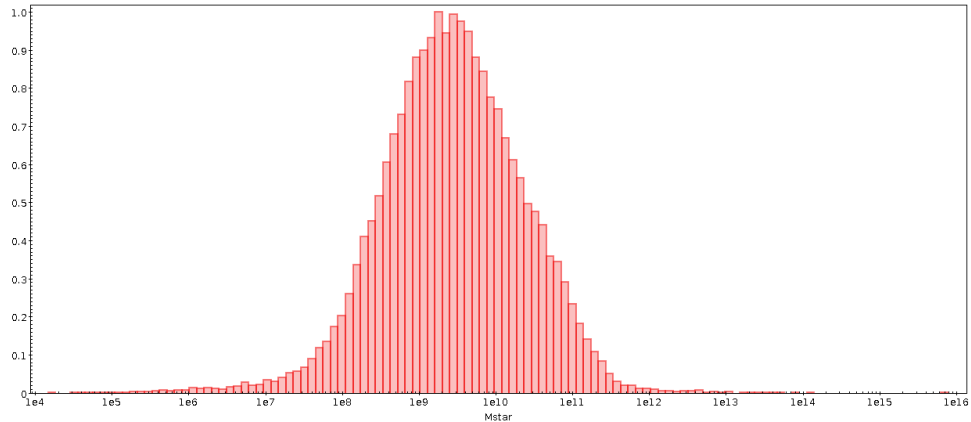


**Figure 3.3:** Distribution of the stellar masses of all galaxies with a SED fit. The bins have been normalized by the count in the largest bin.

3.2. The distribution of the stellar masses of all fitted galaxies is shown in figure 3.3.

### Main sequence SFR

To determine the specific star formation rate in units of the specific star formation rate of main sequence galaxies ( $sSFR_{ms}$ ), this work uses the same definition of the main sequence as given by Lee et al. (2015) with no evolution beyond  $z=2.5$ . This is the same definition as used by Scoville et al. (2016) to enable a direct comparison between their results and this work.

#### 3.2.4 Stacking methods

For the ALESS data the same stacking method as described in the previous chapter is used. A weighed mean stacking method where the weight is determined by the distance from the pointing center of the observation. For the LESS and HerMES data the global deblending method is used.

#### 3.2.5 Molecular gas masses

From the stacked submillimeter fluxes, a molecular gas mass can be derived using the method described in the introduction. Specifically, equation 1.8 can be used to go from flux in mJy to molecular gas mass. It should be noted that Scoville et al. (2016) advise that this relation is not used beyond  $\lambda_{rest} \gtrsim 250\mu\text{m}$ . For ALESS and LESS at  $870\mu\text{m}$  this corresponds to

$z \sim 2.5$  and for *Herschel* SPIRE 500 $\mu\text{m}$  this the cut-off is only at  $z \sim 1.0$ . It should be noted that in this work, for some redshift cuts, the limits are being pushed beyond what is recommended.

The molecular gas mass derived from the stacked fluxes and the stellar masses from the optical-NIR SED fitting can be used to estimate the gas fraction of the stacked galaxies:

$$f_{\text{gas}} = \frac{M_{\text{mol}}}{M_{\text{mol}} + M_*} \quad (3.2)$$

The mass ratio between stellar mass and gas mass is also used as a way to interpret of the amount of gas in a galaxy:

$$R_{\text{mass}} = \frac{M_{\text{mol}}}{M_*} \quad (3.3)$$

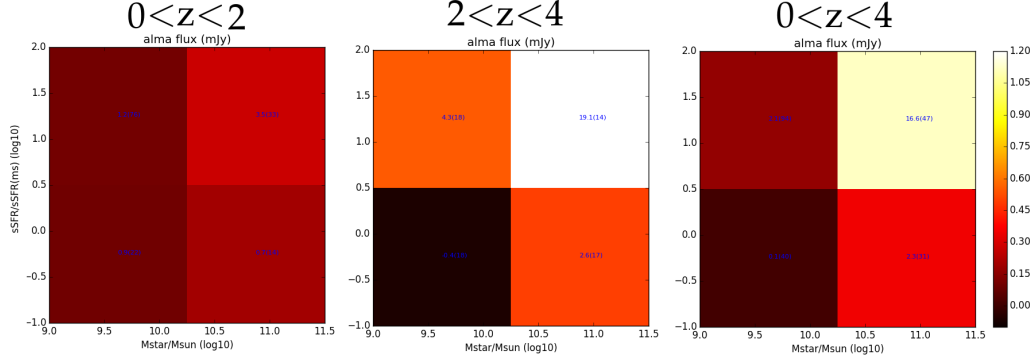


**Figure 3.4:** Stacked flux for different stellar mass and  $sSFR_{ms}$  bins. The colorscale for all subfigures is the same. The redshift cut is indicated above the subfigure. The blue numbers indicate the SNR and the number of galaxies in that stack is also given in parentheses.

## 3.3 Results

### 3.3.1 ALESS

Firstly a stacking analysis on galaxies in bins of stellar mass and  $sSFR_{ms}$  is used to produce a figure similar to figure 3.1 from Scoville et al. (2016). Two redshift cuts are used, one contains sources with  $0 < z < 2$  and the high redshift cut contains galaxies with  $2 < z < 4$ . An additional cut that covers the complete redshift range  $0 < z < 4$  is also stacked. The results are shown in figure 3.4, 3.5 and 3.6.

Because of the low number of galaxies in each bin, it is interesting to only stack on just one physical parameter instead of two. In the remainder of this section a stacking analysis will be done on galaxies in bins of increasing stellar mass and also on bins of increasing  $sSFR_{ms}$ . These stacking analyses will be done for the same redshifts cuts as the previous analysis.

### 3.3.2 LESS and HerMES

It is observed that stacked galaxies  $\lesssim 10^{10} M_\odot$  do not give rise to significant detections. The stacked fluxes are often even negative. Therefore these galaxies will be excluded from the stacking analysis of LESS and HerMES. Specifically, the following stacking analysis only considers galaxies with  $10^{10} M_\odot \leq M_* \leq 10^{11.5} M_\odot$  and  $10^{-1} \leq sSFR_{ms} \leq 10^2$ .

Again different redshift cuts are used, because of the large number of galaxies available for the stacking analysis, it is possible to make more

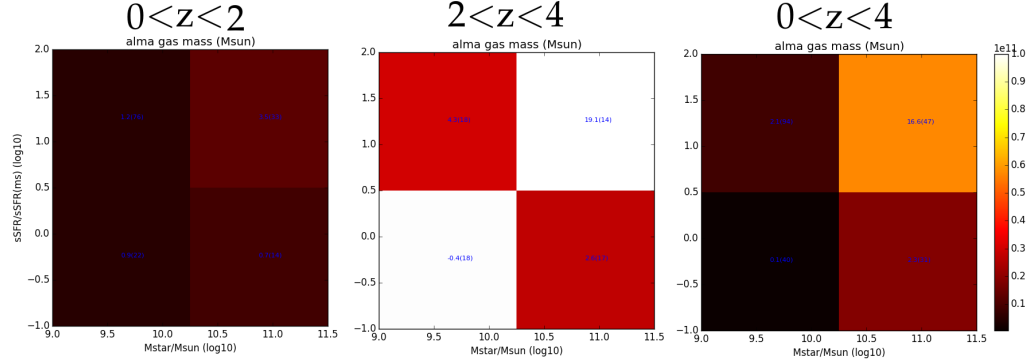


**Figure 3.5:** Molecular mass derived from the stacked flux for different stellar mass and  $sSFR_{ms}$  bins. The colorscale for all subfigures is the same. The redshift cut is indicated above the subfigure. The blue numbers indicate the SNR and the number of galaxies in that stack is also given in parentheses.

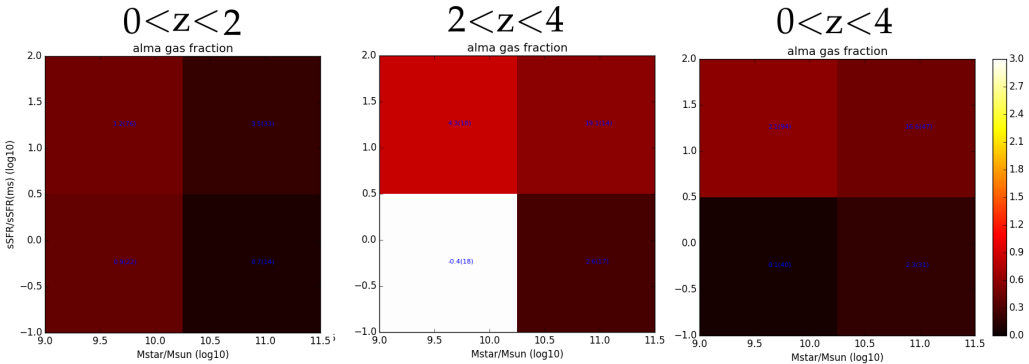


**Figure 3.6:** Gas fraction for different stellar mass and  $sSFR_{ms}$  bins. The colorscale for all subfigures is the same. The redshift cut is indicated above the subfigure. The blue numbers indicate the SNR and the number of galaxies in that stack is also given in parentheses.

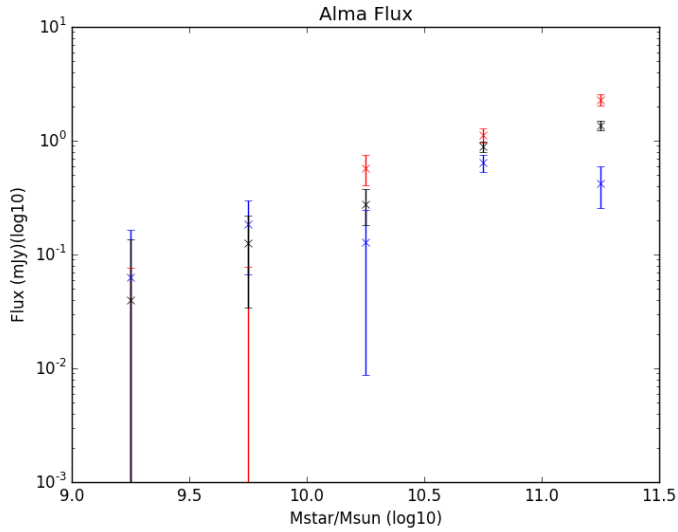


**Figure 3.7:** Stacked flux for different bins of stellar mass. The stacked flux of three redshift cuts are shown,  $0 < z < 2$  (blue),  $2 < z < 4$  (red) and  $0 < z < 4$  (black).

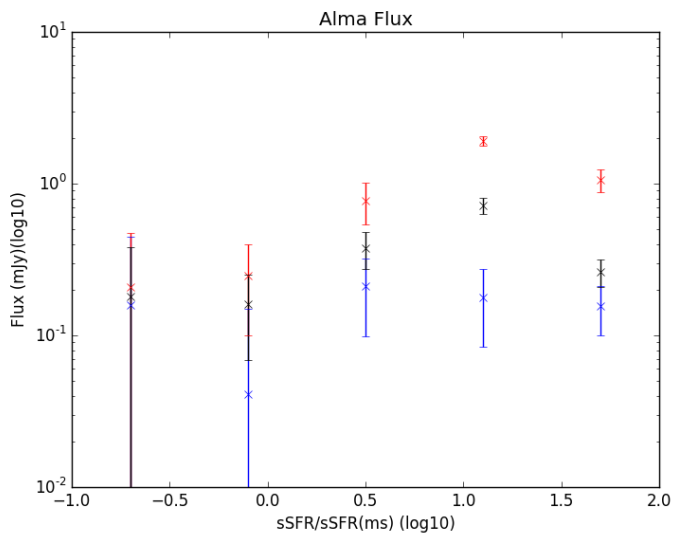


**Figure 3.8:** Stacked flux for different bins of  $sSFR_{ms}$ . The stacked flux of three redshift cuts are shown,  $0 < z < 2$  (blue),  $2 < z < 4$  (red) and  $0 < z < 4$  (black).

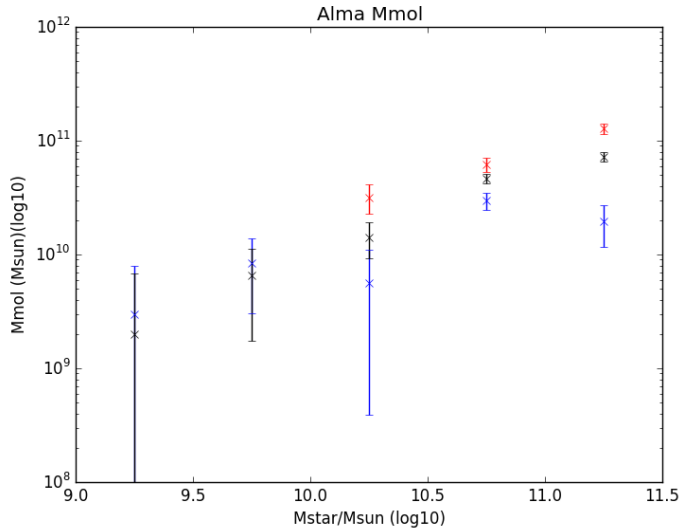


**Figure 3.9:** Molecular masses derived from the stacked fluxes shown in figure 3.7. The molecular masses determined for three redshift cuts are shown,  $0 < z < 2$  (blue),  $2 < z < 4$  (red) and  $0 < z < 4$  (black).

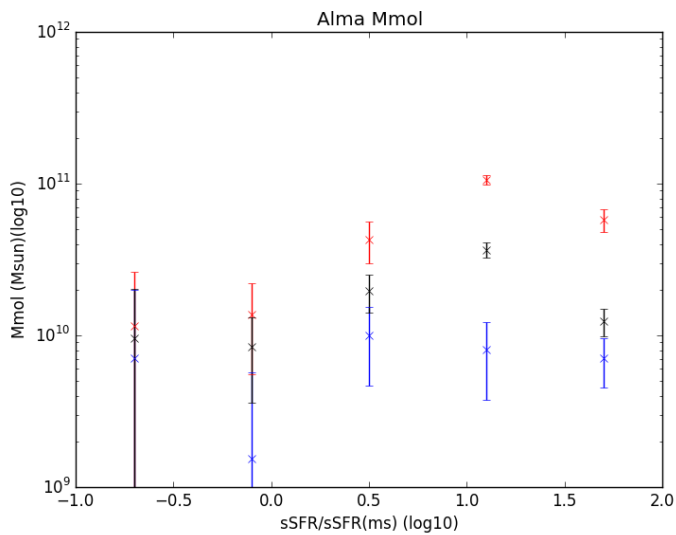


**Figure 3.10:** Molecular masses derived from the stacked fluxes shown in figure 3.8. The molecular masses determined for three redshift cuts are shown,  $0 < z < 2$  (blue),  $2 < z < 4$  (red) and  $0 < z < 4$  (black).

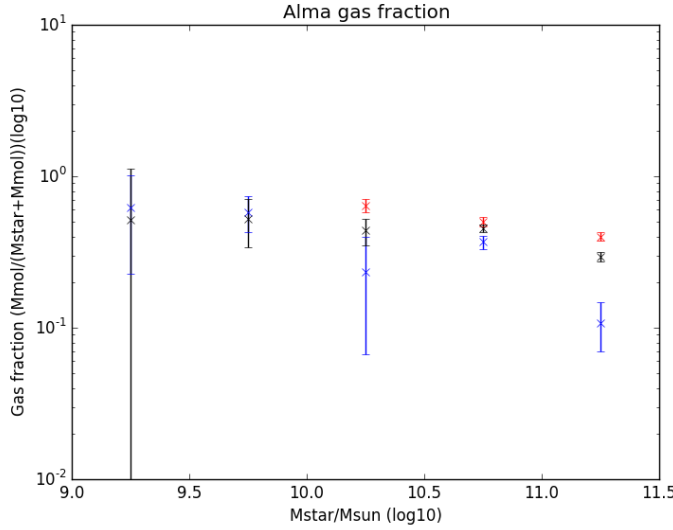


**Figure 3.11:** Gas fraction derived from the stacked fluxes shown in figure 3.7. The gas fractions of three redshift cuts are shown,  $0 < z < 2$  (blue),  $2 < z < 4$  (red) and  $0 < z < 4$  (black). The errorbars on the datapoints only accounts for errors in the stacked fluxes, the error in stellar mass is ignored.

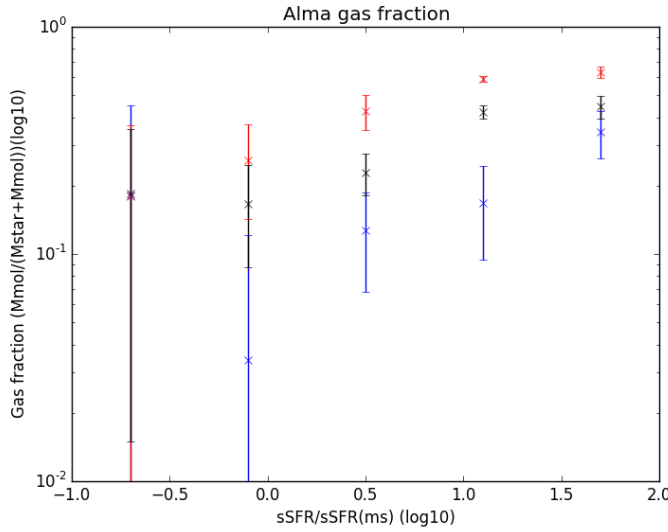


**Figure 3.12:** Gas fraction derived from the stacked fluxes shown in figure 3.8. The gas fractions of three redshift cuts are shown,  $0 < z < 2$  (blue),  $2 < z < 4$  (red) and  $0 < z < 4$  (black). The errorbars on the datapoints only accounts for errors in the stacked fluxes, the error in stellar mass is ignored.

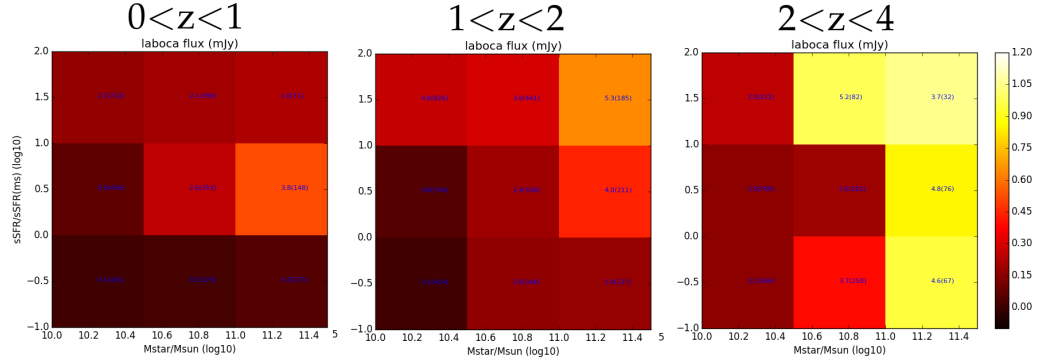


**Figure 3.13:** Stacked LESS flux for different stellar mass and  $sSFR_{ms}$  bins. The colorscale for all subfigures is the same. The redshift cut is indicated above the subfigure. The blue numbers indicate the SNR and the number of galaxies in that stack is also given in parentheses.

refined redshift cuts. For the stacking on bins of stellar mass and  $sSFR_{ms}$ , the following redshift cuts are used:  $0 < z < 1$ ,  $1 < z < 2$  and  $2 < z < 4$ . The results are shown below.

Again, it is interesting to stack on bins with a single physical parameter, basically collapsing all data points onto a single axis. This will be done for both the stellar mass and the  $sSFR_{ms}$ . Because of the increased number of galaxies in each bin, more refined redshift cuts are possible. The used redshift cuts and the colours of the corresponding data-points are:  $0 < z < 0.5$  (blue),  $0.5 < z < 1$  (green),  $1 < z < 1.5$  (yellow),  $1.5 < z < 2$  (orange) and  $2 < z < 4$  (red). Additionally, the complete redshift range is stacked  $0 < z < 4$  (black).

Figures 3.19 to 3.30 can be transformed to plots with the gas fraction as a function of redshift. Individual data points are color-coded for increasing stellar mass or  $sSFR_{ms}$ . The gas fractions derived by this work can be put into context using a compilation of gas fractions derived by previous studies from Decarli et al. (2016). These studies used CO instead of a continuum based determination of the gas fraction. The result is shown in the figures 3.31 to 3.36, first looking at stellar mass and next at  $sSFR_{ms}$ . The grey line in these figures is given by  $f_{\text{gas}} = 1/(1 + 1/R_{\text{mass}})$  where  $R_{\text{mass}} = 0.1 \cdot (1 + z)^2$  (Geach et al. 2011; Magdis et al. 2012).

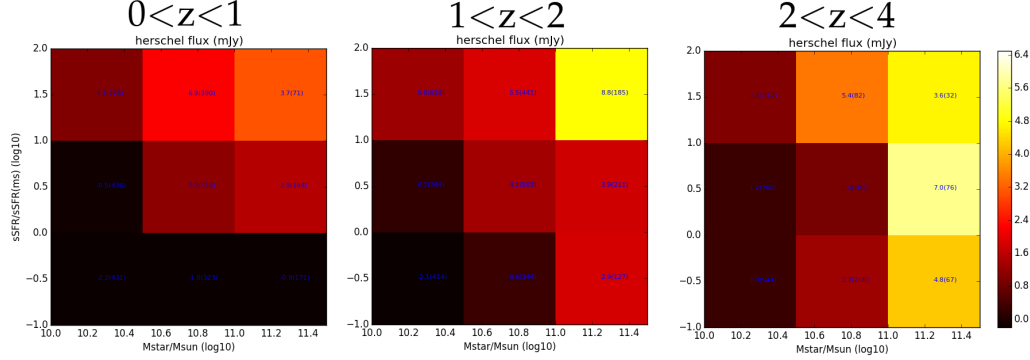


**Figure 3.14:** Stacked HerMES flux for different stellar mass and  $sSFR_{ms}$  bins. The colorscale for all subfigures is the same. The redshift cut is indicated above the subfigure. The blue numbers indicate the SNR and the number of galaxies in that stack is also given in parentheses.

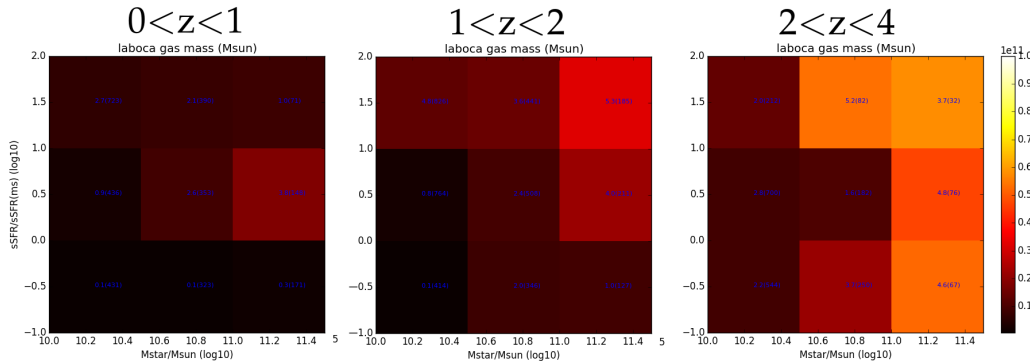


**Figure 3.15:** Molecular mass derived from the stacked LESS flux for different stellar mass and  $sSFR_{ms}$  bins. The colorscale for all subfigures is the same. The redshift cut is indicated above the subfigure. The blue numbers indicate the SNR and the number of galaxies in that stack is also given in parentheses.

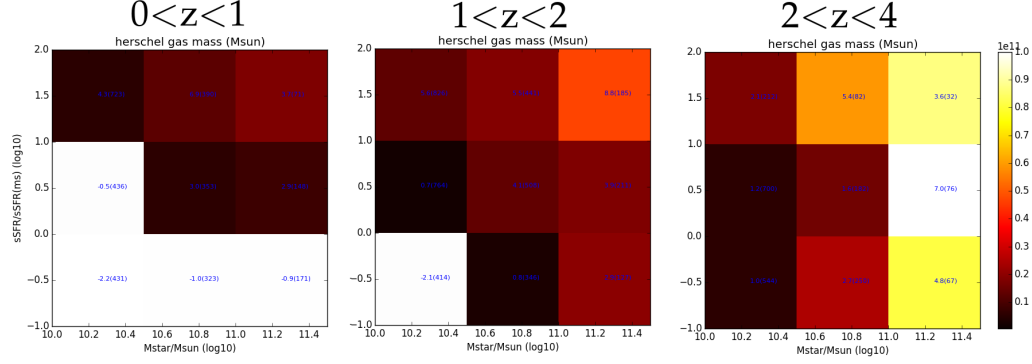


**Figure 3.16:** Molecular mass derived from the stacked HerMES flux for different stellar mass and  $sSFR_{ms}$  bins. The colorscale for all subfigures is the same. The redshift cut is indicated above the subfigure. The blue numbers indicate the SNR and the number of galaxies in that stack is also given in parentheses.

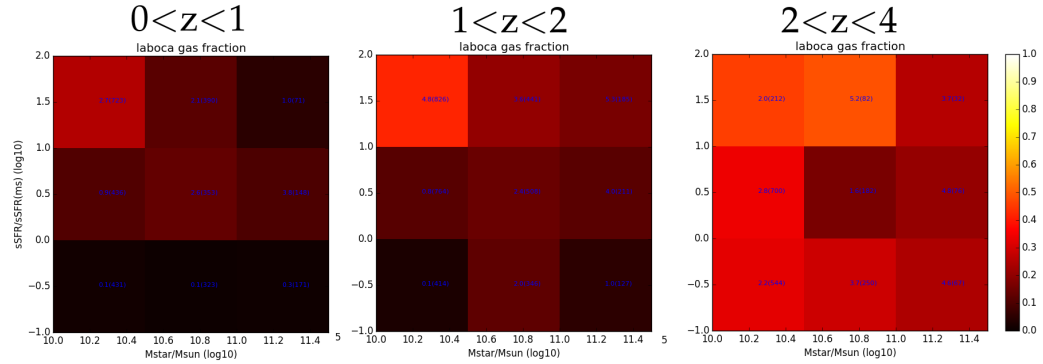


**Figure 3.17:** Gas fraction for different stellar mass and  $sSFR_{ms}$  bins. The colorscale for all subfigures is the same. The redshift cut is indicated above the subfigure. The blue numbers indicate the SNR and the number of galaxies in that stack is also given in parentheses.

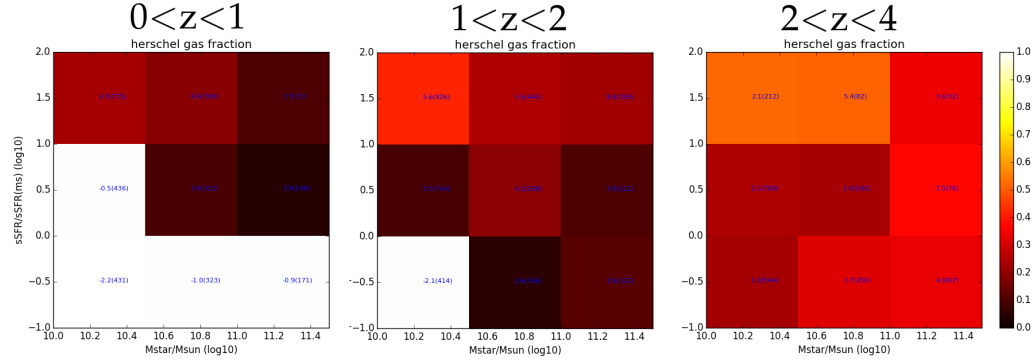


**Figure 3.18:** Gas fraction for different stellar mass and  $s\text{SFR}_{ms}$  bins. The colorscale for all subfigures is the same. The redshift cut is indicated above the subfigure. The blue numbers indicate the SNR and the number of galaxies in that stack is also given in parentheses.

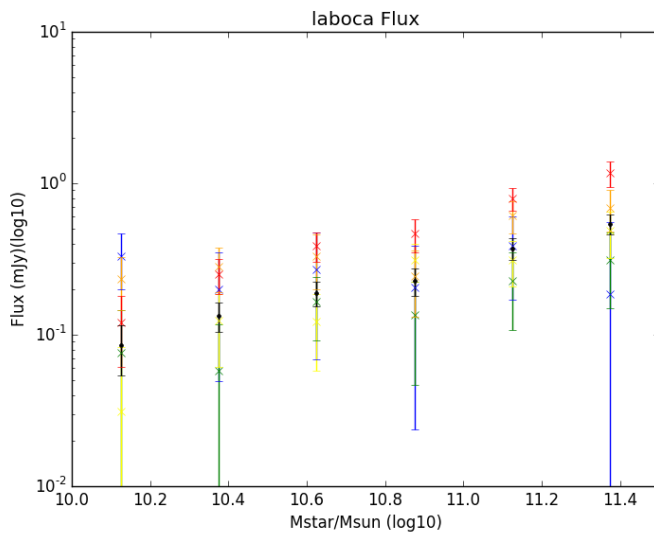


**Figure 3.19:** Stacked LESS flux for a number of stellar mass bins. The colors of the datapoints refer to different redshift cuts (see section 3.3.2). The black datapoint is derived from a stack on the complete redshift range.

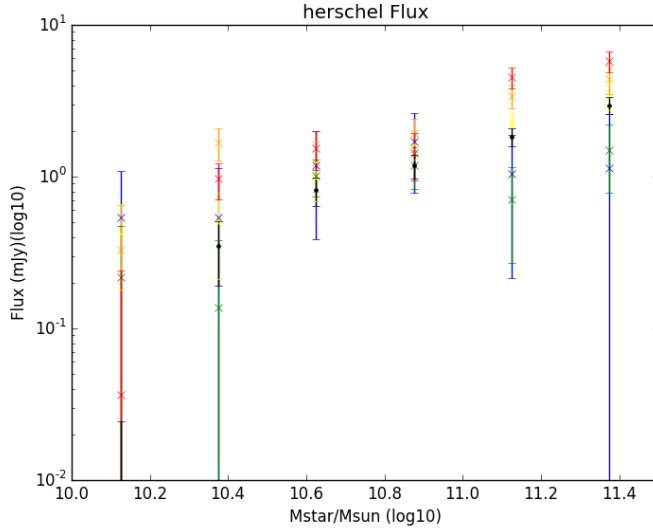


**Figure 3.20:** Stacked HerMES flux for a number of stellar mass bins. The colors of the datapoints refer to different redshift cuts (see section 3.3.2). The black datapoint is derived from a stack on the complete redshift range.

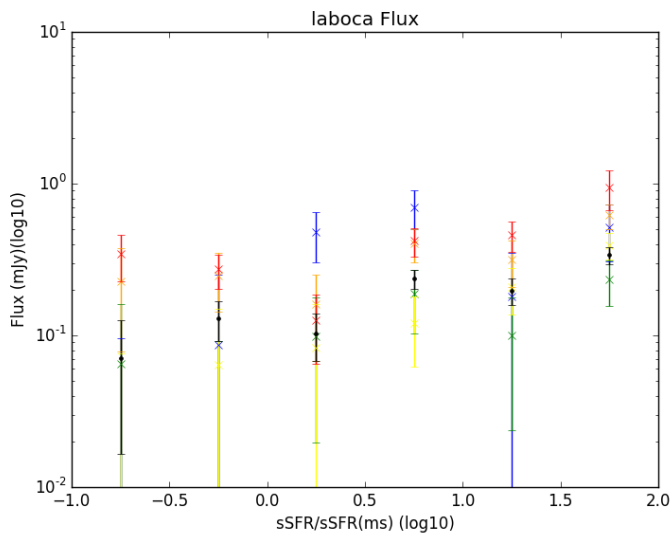


**Figure 3.21:** Stacked LESS flux for bins of increasing  $sSFR_{ms}$ . The colors of the datapoints refer to different redshift cuts (see section 3.3.2). The black datapoint is derived from a stack on the complete redshift range.

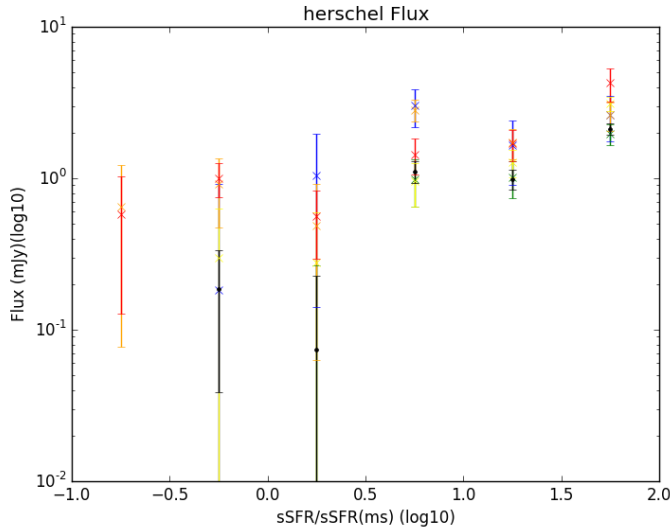


**Figure 3.22:** Stacked HerMES flux for bins of increasing  $sSFR_{ms}$ . The colors of the datapoints refer to different redshift cuts (see section 3.3.2). The black datapoint is derived from a stack on the complete redshift range.

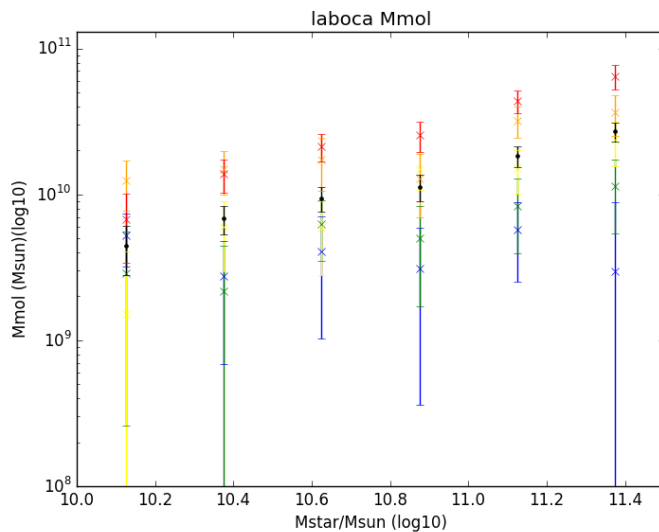


**Figure 3.23:** Molecular gas mass derived from the stacked LESS fluxes for bins with increasing stellar mass. The colors of the datapoints refer to different redshift cuts (see section 3.3.2). The black datapoint is derived from a stack on the complete redshift range.

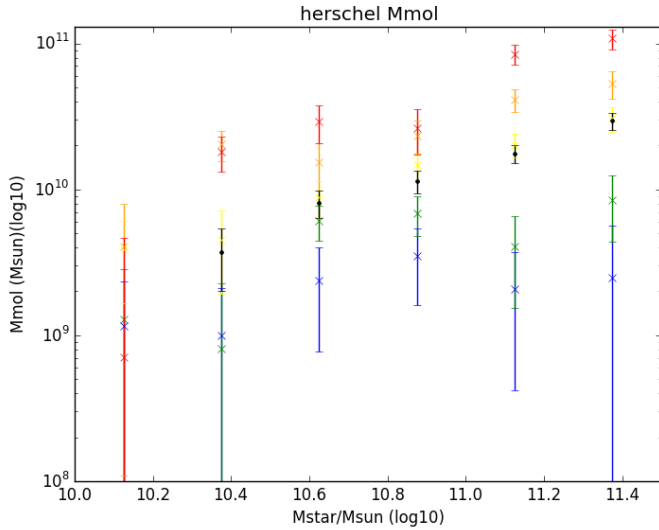


**Figure 3.24:** Molecular gas mass derived from the stacked HerMES fluxes for bins with increasing stellar mass. The colors of the datapoints refer to different redshift cuts (see section 3.3.2). The black datapoint is derived from a stack on the complete redshift range.

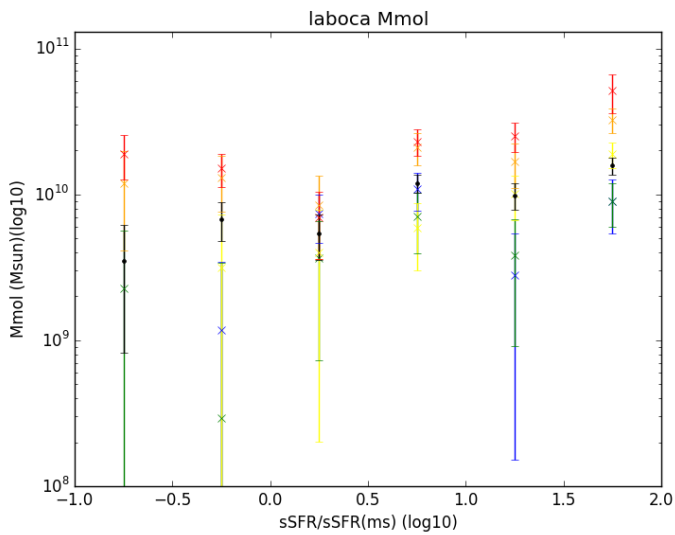


**Figure 3.25:** Molecular gas mass derived from the stacked LESS fluxes for bins with increasing  $ssFR_{ms}$ . The colors of the datapoints refer to different redshift cuts (see section 3.3.2). The black datapoint is derived from a stack on the complete redshift range.

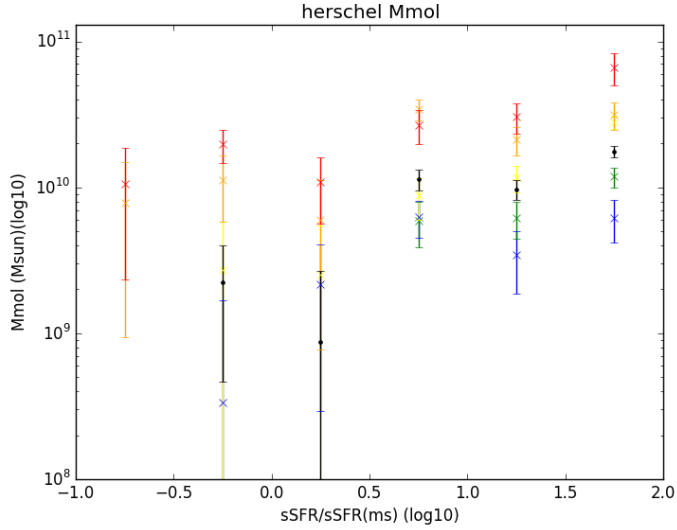


**Figure 3.26:** Molecular gas mass derived from the stacked LESS fluxes for bins with increasing  $ssFR_{ms}$ . The colors of the datapoints refer to different redshift cuts (see section 3.3.2). The black datapoint is derived from a stack on the complete redshift range.

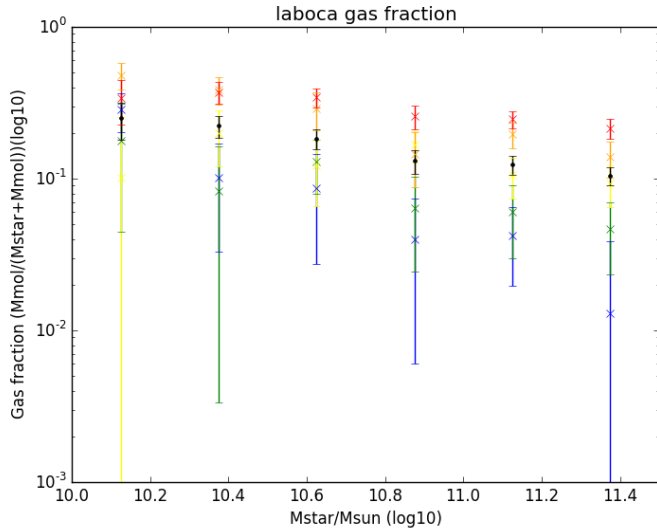


**Figure 3.27:** Gas fraction for bins with increasing stellar mass. The colors of the datapoints refer to different redshift cuts (see section 3.3.2). The black datapoint is derived from a stack on the complete redshift range.

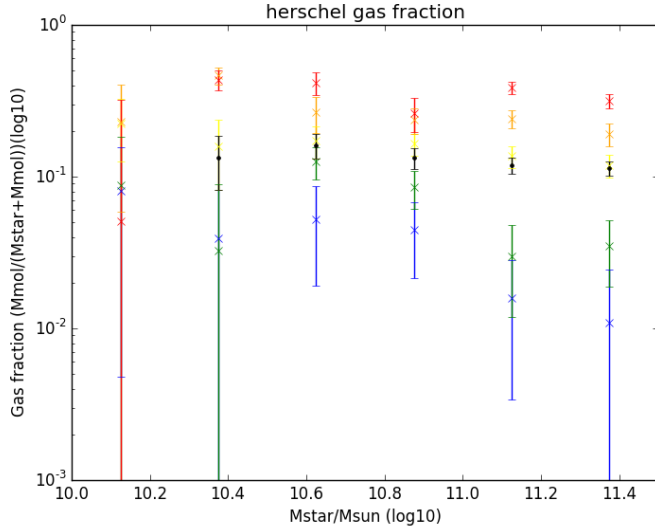


**Figure 3.28:** Gas fraction for bins with increasing stellar mass. The colors of the datapoints refer to different redshift cuts (see section 3.3.2). The black datapoint is derived from a stack on the complete redshift range.

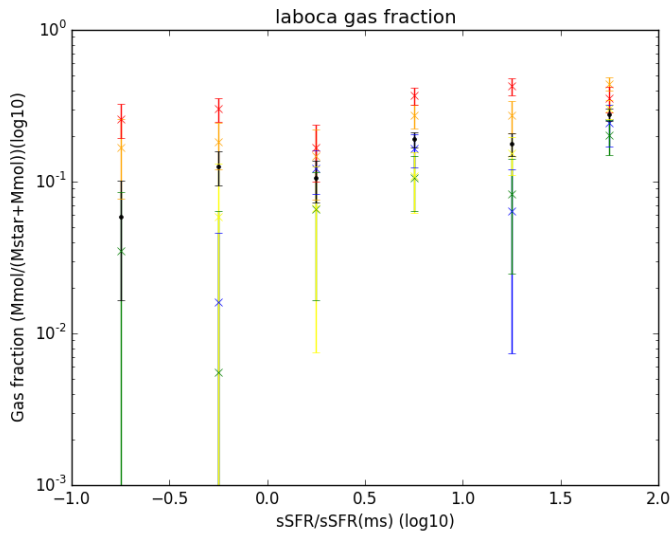


**Figure 3.29:** Gas fraction for bins of galaxies with a increasing  $sSFR_{ms}$ . The colors of the datapoints refer to different redshift cuts (see section 3.3.2). The black datapoint is derived from a stack on the complete redshift range.

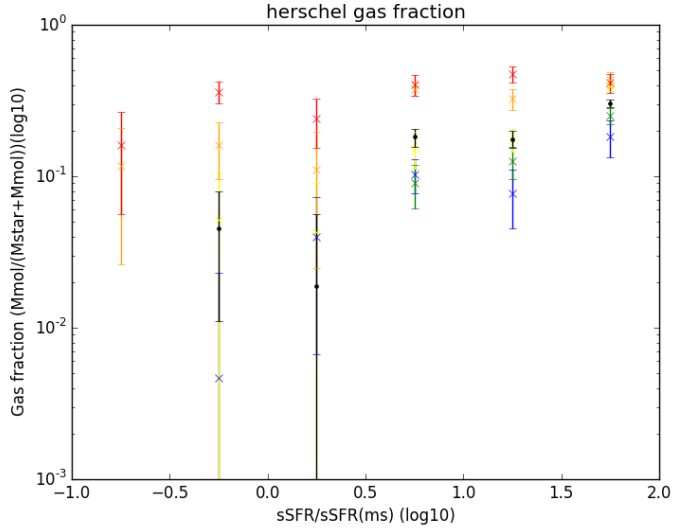


**Figure 3.30:** Gas fraction for bins of galaxies with a increasing  $sSFR_{ms}$ . The colors of the datapoints refer to different redshift cuts (see section 3.3.2). The black datapoint is derived from a stack on the complete redshift range.

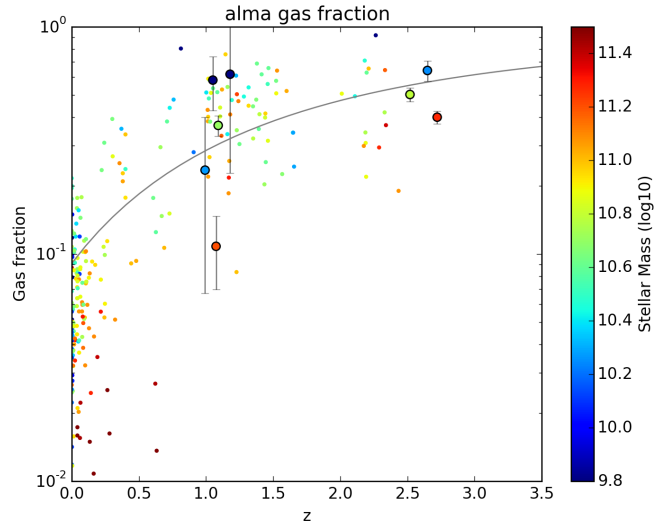


**Figure 3.31:** Gas fraction for two redshift cuts ( $0 < z < 2$  and  $2 < z < 4$ ), the position of the cut on the x-axis is determined by the average redshift of the galaxies in that cut. Datapoints are color-coded according to the average stellar mass of the galaxies in the stack corresponding to that datapoint. The colored points in the background are obtained from a compilation by Decarli et al. (2016).

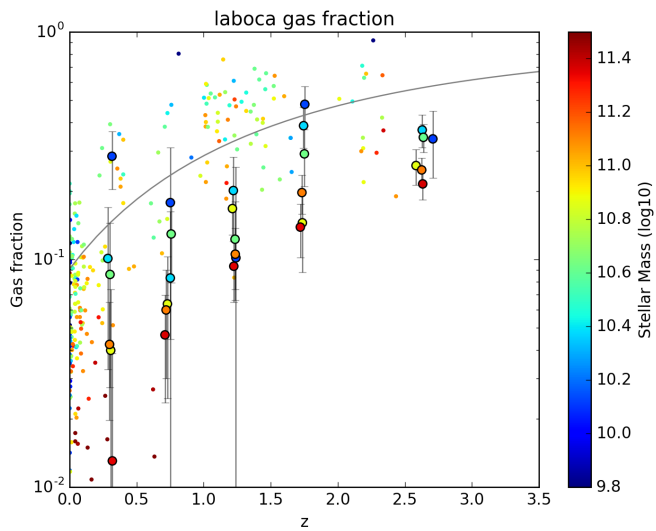


**Figure 3.32:** Same as figure 3.31, but for stacking on the LESS survey and with more redshift cuts as described in section 3.3.2.

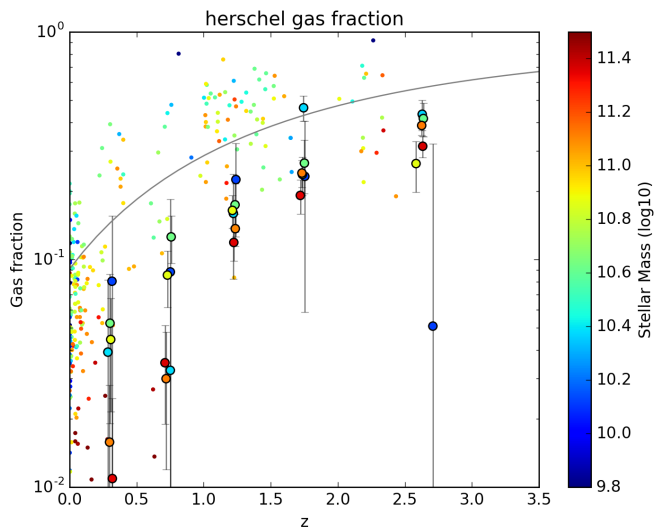


**Figure 3.33:** Same as figure 3.31, but for stacking on the HerMES survey and with more redshift cuts as described in section 3.3.2.

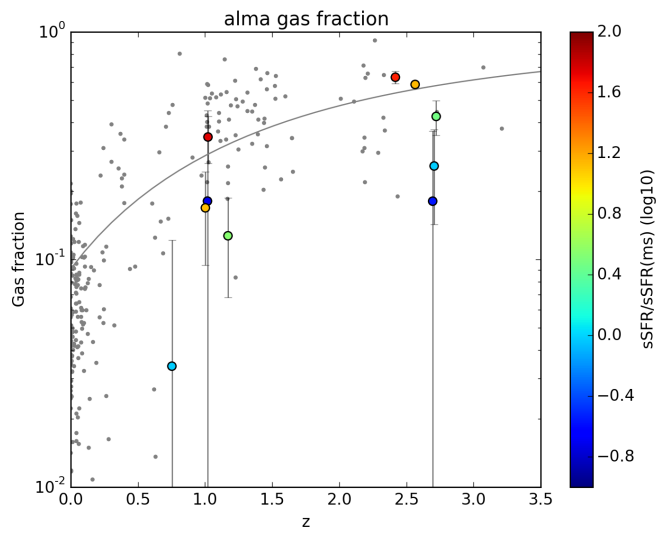


**Figure 3.34:** Same as figure 3.31, but galaxies are binned according to their  $sSFR_{ms}$  instead of stellar mass.

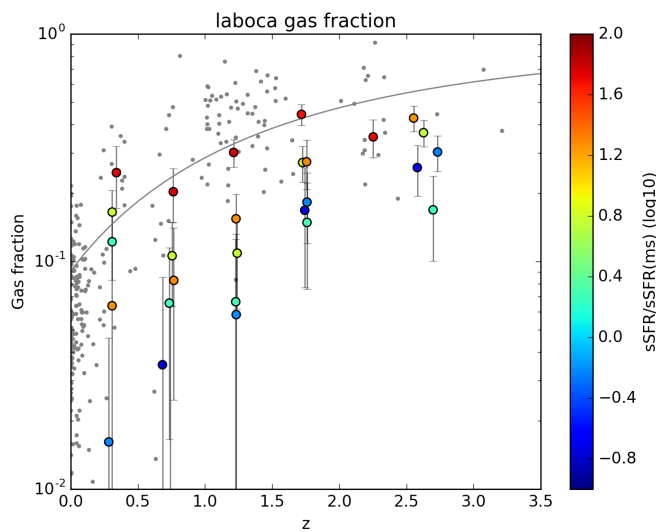


**Figure 3.35:** Same as figure 3.32, but galaxies are binned according to their  $sSFR_{ms}$  instead of stellar mass.

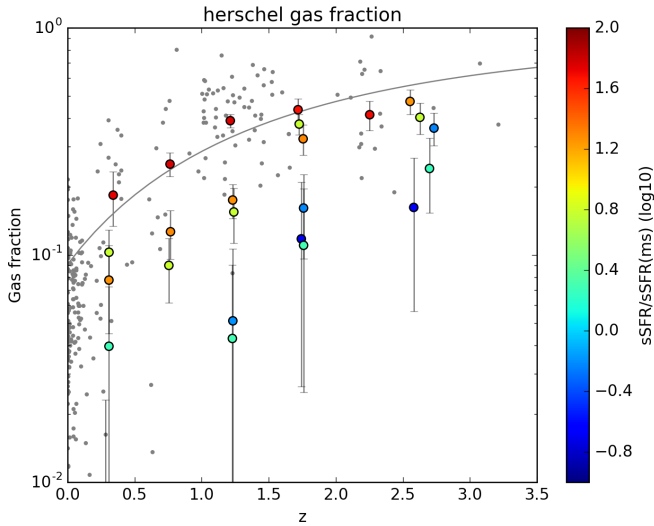


**Figure 3.36:** Same as figure 3.33, but galaxies are binned according to their  $sSFR_{ms}$  instead of stellar mass.

## 3.4 Discussion

### 3.4.1 Grid binning

As discussed in the beginning of this chapter, Scoville et al. (2016) has determined the gas fraction for galaxies in a grid of bins of stellar mass and  $sSFR_{ms}$ , see the bottom row of figure 3.1. Scoville et al. (2016) also used this figure to fit a function (equation 3.1) which gives the gas fraction as a function of stellar mass,  $sSFR_{ms}$  and redshift.

In this work, a two dimensional grid of binned galaxies for stellar mass and  $sSFR_{ms}$  has also been used for a stacking analysis on ALESS, LESS and HerMES data. The resulting gas fractions are shown in figures 3.6, 3.17 and 3.18 respectively.

From these figures it is clear that the gas fraction of the stacked galaxies increases with redshift. Moreover, galaxies with a lower stellar mass tend to have a higher gas fraction. The opposite is true for galaxies with a low  $sSFR_{ms}$  which tend to have lower gas fractions. This is also visible in figure 3.1 from Scoville et al. (2016).

It should be noted that the HerMES 500 $\mu$ m data are being used beyond the recommended redshift limit, this is even the case for the ALESS and LESS data beyond  $z \sim 2.5$ . However, the effects of this transgression do not seem to be very extreme. The ALESS, LESS and HerMES data give

similar results for the redshift range  $1 < z < 2$ . Although for that redshift range, the HerMES restframe wavelength is already beyond  $250\mu\text{m}$  (which is recommended by Scoville et al. (2016)), while the ALESS and LESS data are not.

Finally, concerning binning on a rectangular grid, the number of sources in each bin vary significantly. It is possible to imagine a scheme where the stellar mass versus  $sSFR_{ms}$  plane is divided in such a way that every cell contains a certain number of sources. Greve et al. (2010) tested such a binning scheme with an adaptive grid, albeit in a different context, and found that it did not have a significant influence on the results of their stacking analysis.

### 3.4.2 Stellar mass dependence

To obtain more insight in the dependence of the gas fraction on stellar mass and  $sSFR_{ms}$  a stacking analysis is performed where the galaxies are binned in only one variable. For more details see the previous section. The results for binning galaxies using bins of stellar mass is shown in figures 3.11 (ALESS), 3.27 (LESS) and 3.28 (HerMES).

From these figures, it is clear that the gas fraction increases with redshift. Moreover, for the complete sample, a trend is visible where the gas fraction decreases for increasing stellar mass. Tacconi et al. (2013) found the same trend and it has also been found by Scoville et al. (2016). However the slope from the fit in equation 3.1 is much less steep, nearly constant.

It should be noted that Scoville et al. (2016) obtained this fit figure 3.1 using a multi-parameter fit, whereas the figures discussed in this section collapse all allowed values of  $sSFR_{ms}$  into the used bins of stellar mass. However, this is equivalent to integrating equation 3.1 along  $sSFR_{ms}$ , which results in a constant factor, preserving the power-law dependence on stellar mass. Of course, this is only true if the integral of  $sSFR_{ms}$  does not strongly depend on star formation rate, which would not be expected, since it this variable has been normalized with the main sequence, which should remove any mass dependence.

However, galaxies with a high  $sSFR_{ms}$  are more easily detected than with galaxies with a lower  $sSFR_{ms}$  this is specifically true for the low mass range. In the low mass range, galaxies with a high  $sSFR_{ms}$  give a larger contribution to the stacked flux, at least if one believes that galaxies with a higher  $sSFR_{ms}$  also have a higher gas fraction. Hence, this results in a bias where star forming galaxies exert a big influence on the lower mass

ranges. This increases the observed steepness of the gas fraction versus stellar mass dependence. Consequently, it would be better to use a much smaller range of  $sSFR_{ms}$  for such a plot.

There is another aspect to the slope of the dependence of the gas fraction on stellar mass. There might be a redshift dependence which is very tentatively visible in all datasets. Specifically, it seems that galaxies with a higher stellar mass experience a larger evolution in gas fraction for increasing redshift than galaxies with a lower stellar mass.

It is also observed that the gas fractions derived from LESS and HerMES are lower than the ALESS gas fraction. This is probably be due to the selection bias at the basis of the ALESS dataset. ALESS is a follow-up of bright submillimeter sources detected in LESS. Consequently, because the ALESS fields are centered on bright submillimeter sources, it is not surprising that the stacked fluxes and subsequently the derived gas fractions are higher than found by LESS and HerMES which are not biased in such a way. Moreover, the same effect has been observed in the previous chapter for the stacking analysis on color selected galaxies. There too the ALESS stacked fluxes are higher than the stacked fluxes from LESS.

### 3.4.3 Dependence on $sSFR_{ms}$

For binning with bins of  $sSFR_{ms}$ , the results are shown in figures 3.12 (ALESS), 3.30 (LESS), and 3.30 (HerMES).

Again it is observed that the gas fraction increases with redshift. The black datapoints, which use the complete redshift range, show that the gas fraction increases for bins with higher  $sSFR_{ms}$  for all datasets.

It is more difficult to get a grip on the slope of the dependence of the gas fraction on  $sSFR_{ms}$ . Though it clear that the slope is generally less steep than the slope derived by Scoville et al. (2016). The slope correspond to a power-law index of about  $\sim 0.3$  or equivalently, about an order of magnitude increase in gas fraction for the  $sSFR_{ms}$  used for this work. It seems that only at low redshifts, such a steep dependence is appropriate, for higher redshifts, the gas fraction seems to be universally higher. Though the errorbars on the lower redshift bins are very big and only allow tentative conclusions.

This changing slope could also be interpreted as a different evolution for galaxies with different  $sSFR_{ms}$ . Specifically, it seems that highly star forming galaxies always have a relatively high gas fraction, whereas the gas fraction of less star forming galaxies have experienced a strong evolution in their gas fractions.

Again it should be noted that this plot effectively integrates the fit from Scoville et al. (2016) over a large mass range. However the dependence of the gas fraction on stellar mass is much less strong than for the  $sSFR_{ms}$ . Consequently, the bias from massive galaxies on the stacked flux should be less severe than the bias from galaxies with a large  $sSFR_{ms}$  described in the previous section.

### 3.4.4 Comparison with CO based gas fractions

The gas fractions of galaxies are most often determined using observations of CO rotational transitions, a compilation of such measurements as a function of redshift (Decarli et al. 2016) was used to put the gas fraction measured by this work into context. The result is shown in figures 3.31 and 3.34 (ALESS), 3.32 and 3.35 (LESS) and 3.33 and 3.36 (HerMES). (These figures use the same data as the figures discussed in the previous sections on the dependence of the gas fraction on stellar mass and  $sSFR_{ms}$ , but presented in a different way.)

From these figures it is clear that here is a difference between the gas fractions as determined from CO based methods and the gas fractions determined in from this work, which uses a continuum dust based method. The offset corresponds to a factor  $\sim 2.5 - 3$  underestimation of the molecular gas mass as determined in this work. Albeit for the ALESS stacking results the discrepancy is much smaller, if not absent. Though, it should be noted that ALESS is biased towards higher stacked fluxes (see also Decarli et al. (2014) and the discussion above).

This difference between the molecular mass as determined through methods using CO lines and continuum based methods has been observed by other works, for example Decarli et al. (2016), who compared the CO line measurements and dust continuum measurements of 6 galaxies in the ALMA Spectroscopic Survey (ASPECS) (Walter et al. 2016). This study uses the same empirical relation between submillimeter flux and molecular gas mass as this work (1.8) from Scoville et al. (2016) and find a comparable discrepancy of a factor  $\sim 3$ .

Decarli et al. (2016) speculate that the discrepancy might be explained by undetected low surface brightness dust continuum emission. The synthesised beam of ASPECS is comparable to the ALESS beam. However, with their much larger beams, LESS and HerMES would have detected this emission, yet the discrepancy remains also for the stacking analysis on these surveys.

There seems to be a systematic difference between the gas masses de-

termined through methods using dust continuum emission and methods using CO lines. Both methods depend on a number of assumptions. For methods based on CO line measurements, the CO-to-H<sub>2</sub> conversion and extrapolations to higher order rotational transitions must be used. Dust based methods rely on a assumed dust temperature, dust spectral index and dust-to-gas ratio, in addition to relying on optically thin conditions. Moreover, the dust continuum methods are often calibrated using CO observations.

If the reason for the discrepancy cannot be attributed to one of these assumptions, it could be argued that the CO based methods are more sensitive to selection biases than the stacking method described in this work. Comparably to the ALESS stacking result, which is biased for brighter galaxies and is more or less consistent with the results from CO line studies, CO studies could be biased for CO bright sources.

From figures 3.35 and 3.36 it can be seen that for both LESS and HERMES, the bins with the highest star formation rates are situated most closely to the CO based datapoints. The same is observed from the ALESS data, the galaxies with the highest  $sSFR_{ms}$  are more consistent with the CO results. This is interesting because the CO based studies used main sequence galaxies (Carilli & Walter 2013). This indicates that a wrong assumption is more likely than a intractable systematic bias for CO based mass determinations.

## 3.5 Conclusion

This chapter looked at the gas fraction in galaxies binned for different values of their stellar mass and  $sSFR_{ms}$ . A dust continuum flux to molecular mass conversion is used, where the flux is determined from a stacking analysis on different submillimeter surveys. It is observed that the different surveys give consistent results.

A clear trend for an increasing gas fraction for increasing redshift is observed. It is observed that the gas fraction drops with increasing stellar mass, though this dependence is biased by galaxies with a large  $sSFR_{ms}$ . The results also show that galaxies with a larger  $sSFR_{ms}$  have a higher gas fraction. All these trends are consistent largely with the literature. A detailed determination of the slope of these dependencies could be the subject of future work.

Additionally, data contain tentative evidence for a separate evolution for galaxies with different stellar masses and  $sSFR_{ms}$ . This difference would lead to an evolution in the slope of the previously discussed dependencies.

Finally, a discrepancy between the molecular gas masses determined by CO line based methods and dust continuum methods is observed. This difference has been observed before. It is likely that this discrepancy can be attributed incorrect assumptions underlying the methods. Future work will be necessary to determine the correct approach to measure molecular masses.



## Conclusion

In this research, stacking analysis was used to look at a variety of galaxies. First color selected galaxies were investigated, this confirmed results from previous studies. Moreover, it demonstrated the effectiveness of the stacking methods, especially the global deblending method.

Next, the physical properties of a large number of galaxies were determined using SED fitting on optical and NIR data with MAGPHYS. Using these physical properties, the dependence of the gas fraction on stellar mass and specific star formation rate in units of the specific star formation rate of the main sequence ( $sSFR_{ms}$ ) was investigated. The gas fraction was determined from molecular gas masses obtained from dust continuum method.

It is found that the gas fraction increases with increasing redshift. Also, high mass galaxies seem to have a lower gas fraction than low mass galaxies. It is also observed that the gas fraction increases for galaxies with a higher  $sSFR_{ms}$ . Moreover, there might be tentative evidence that the gas fraction evolves more quickly for galaxies with a large stellar mass and for galaxies with a low  $sSFR_{ms}$ .

When the measured gas fraction was put into context with previous work from CO based methods, it is found that the molecular gas masses are about  $\sim 2.5\text{-}3$  times lower. The origin for this discrepancy might be attributed to one or more of the many assumptions at the basis of CO and dust continuum methods to determine the molecular gas mass.

### 4.0.1 Future work

The results presented in this research are interesting, but tentative. To increase the significance of the results, it could be possible to expand the stacking analysis to more (public) deep submillimeter datasets from *Herschel* or other telescopes.

Considering *Herschel*, it would be interesting to better quantify the consequences of going beyond the recommended redshift range and using the Scoville et al. (2016) gas mass determination method to the edge of the Rayleigh Jeans regime. As the current data do not show serious effects.

In the discussion of chapter 3 the fit from Scoville et al. (2016) was compared with the results from this work. It would however be interesting to reproduce that fit properly with the data presented in this paper.

It might also be possible to look into the redshift dependence of the slopes of that fit, which is connected to the different evolution of different kinds of galaxies. More data would obviously help to lower the errorbars and clarify any trends.

The observed discrepancy between CO and dust continuum based methods to determine the molecular gas mass is very interesting and requires further investigation. What assumptions are wrong or is there another systematic bias?

To make sure that the fluxes determined in chapter 3 by the global deblending method are correct for the catalog used in chapter 3, it might be interesting to redo the analysis with the catalog used in chapter 2. The global deblending method was demonstrated to work properly with this catalog by testing it against the results from Greve et al. (2010). A catalog with many more sources might decrease the stacked fluxes.

Finally, it will be interesting to take a better look at the fitted physical properties. A large number of galaxies was fitted, but the potential of this dataset was not completely used, as it was only used to bin galaxies for further stacking analysis. It could for example be interesting to look at the differences between galaxies close to ALESS sources and galaxies in the general field. That comparison might give more insight in the flux surplus observed when stacking on the ALESS sample. Do galaxies close to bright submillimeter sources have different properties?

## Acknowledgements

First and foremost, I would like to thank dr. Jacqueline A. Hodge, the supervisor of this project, with whom the weekly meetings always were very insightful and helpful.

Also dr. Roberto Decarli who regularly joined the weekly meetings via Skype. His comments and especially the suggestion to look at the work of Scoville et al. were essential for this work.

And finally, dr. Elisabete Da Cunha, the author of MAGPHYS, who I had the pleasure of meeting, and changed MAGPHYS so it could run much faster specifically for this project.



# References

- Avendano, F. P. N. 2015, The APEX submillimeter imaging survey of distant galaxies in the COSMOS field (Dissertation)
- Caillault, J.-P. & Helfand, D. J. 1985, , 289, 279
- Cardamone, C. N., van Dokkum, P. G., Urry, C. M., et al. 2010, , 189, 270
- Carilli, C. L. & Walter, F. 2013, , 51, 105
- Chabrier, G. 2003, , 115, 763
- Cimatti, A., Daddi, E., Cassata, P., et al. 2003, , 412, L1
- da Cunha, E., Charlot, S., & Elbaz, D. 2008, , 388, 1595
- da Cunha, E., Walter, F., Smail, I. R., et al. 2015, , 806, 110
- Daddi, E., Cimatti, A., Renzini, A., et al. 2004, , 617, 746
- Damen, M., Labb  , I., van Dokkum, P. G., et al. 2011, , 727, 1
- Decarli, R., Smail, I., Walter, F., et al. 2014, , 780, 115
- Decarli, R., Walter, F., Aravena, M., et al. 2016, , 833, 70
- Franx, M., Labb  , I., Rudnick, G., et al. 2003, , 587, L79
- Geach, J. E., Smail, I., Moran, S. M., et al. 2011, The Astrophysical Journal Letters, 730, L19
- Georgakakis, A., Hopkins, A. M., Sullivan, M., et al. 2003, , 345, 939
- Greve, T. R., Wei  , A., Walter, F., et al. 2010, , 719, 483

- Hodge, J. A., Karim, A., Smail, I., et al. 2013, , 768, 91
- Hodge, J. A., Swinbank, A. M., Simpson, J. M., et al. 2016, ArXiv e-prints [[arXiv]1609.09649]
- Ilbert, O., Capak, P., Salvato, M., et al. 2009, , 690, 1236
- Kimm, T., Slyz, A., Devriendt, J., & Pichon, C. 2011, , 413, L51
- Kurczynski, P. & Gawiser, E. 2010, , 139, 1592
- Lee, N., Sanders, D. B., Casey, C. M., et al. 2015, , 801, 80
- Lindroos, L., Knudsen, K. K., Fan, L., et al. 2016, , 462, 1192
- Madau, P. & Dickinson, M. 2014, , 52, 415
- Magdis, G. E., Daddi, E., Sargent, M., et al. 2012, *The Astrophysical Journal Letters*, 758, L9
- Noeske, K. G., Weiner, B. J., Faber, S. M., et al. 2007, , 660, L43
- Oliver, S. J., Bock, J., Altieri, B., et al. 2012, , 424, 1614
- Planck Collaboration, Adam, R., Ade, P. A. R., et al. 2016, , 594, A1
- Schreiber, C., Pannella, M., Elbaz, D., et al. 2015, , 575, A74
- Scoville, N., Aussel, H., Sheth, K., et al. 2014, , 783, 84
- Scoville, N., Sheth, K., Aussel, H., et al. 2016, , 820, 83
- Simpson, J. M., Swinbank, A. M., Smail, I., et al. 2014, , 788, 125
- Tacconi, L. J., Neri, R., Genzel, R., et al. 2013, , 768, 74
- Taylor, E. N., Franx, M., van Dokkum, P. G., et al. 2009, , 183, 295
- Thompson, D., Beckwith, S. V. W., Fockenbrock, R., et al. 1999, , 523, 100
- van Dokkum, P. G., Franx, M., Förster Schreiber, N. M., et al. 2004, , 611, 703
- Walter, F., Decarli, R., Aravena, M., et al. 2016, , 833, 67
- Weiß, A., Kovács, A., Coppin, K., et al. 2009, , 707, 1201